Computational investigation of vertical upflow boiling of liquid nitrogen and effects of bubble collision dispersion force

Sunjae Kim [a], Jeongmin Lee [a], Issam Mudawar [a,1,*], Jason Hartwig [b]

[a] Purdue University Boiling and Two-Phase Flow Laboratory (PU-BTPFL), School of Mechanical Engineering, Purdue University, 585 Purdue Mall, West Lafayette, IN 47907, USA

[b] Fluids and Cryogenics Branch, NASA Glenn Research Center, 21000 Brookpark Rd, Cleveland, OH 44135, USA

ARTICLE INFO

ABSTRACT

The present study investigates the performance of 2-D axisymmetric computational fluid dynamics (CFD) in predicting boiling characteristics of liquid nitrogen flowing vertically upwards along a uniformly heated circular tube. Investigation of the popular Volume of Fluid (VOF) model reveals (a) inaccurate surface tension calculation which degrades interface tracking, and (b) under-representation of bubble-to-bubble interaction, which stems from the innate nature of employing a single momentum equation in VOF. To alleviate VOF shortcomings, Coupled Level Set VOF (CLSVOF) is adopted in ANSYS FLUENT, including a user defined function to account for the crucial effects of bubble collision dispersion force. The CFD simulation results are validated against wall temperature and volume fraction results from prior benchmark experiments corresponding to four different wall heat flux conditions at nearly identical mass velocities. Predictions are also provided for axial variations of interfacial flow pattern, fluid temperature, and fluid velocity, flow characteristics that are very difficult to measure in cryogenic experiments. The CFD simulation results are shown to be highly accurate at predicting the nucleate boiling portion of the flow boiling curve.

© 2022 Elsevier Ltd. All rights reserved.

1. Introduction

1.1. Background

1.1.1. Predictive methods for flow boiling in tubes

Researchers have recognized the heat transfer merits of boiling for many decades, evidenced by the prevalence of boiling processes in a vast number of industrial applications, including power generation, chemical, pharmaceutical, and refrigeration and air conditioning, to name a few. Experimental study of boiling phenomena has been a primary focus for investigators at the Purdue University Boiling and Two-Phase Flow Laboratory (PU-BTPFL) since the mid-1980s. A primary objective of these efforts has been to provide a basis for developing predictive methods for virtually all boiling configurations, include capillary-driven [1], pool [2], falling-film [3], macro-channel [4], micro-channel [5,6], jet [7], and spray [8], as well as hybrid schemes [9].

Overall, there are three primary methods to predict transport behavior in boiling: (i) empirical correlations, (ii) theoretical models, and (iii) computational models. Of the three, correlations remain the most widely adopted in most industries for both design and performance assessment, while theoretical models are quite sparse. With vastly improved computer resources, recent years have witnessed an unprecedented surge in use of computational methods to model boiling behavior. The present study is focused on developing an experimentally validated computational model for flow boiling specifically tailored to cryogenic fluids.

1.1.2. Prior experimental and correlation-based cryogenic work

Historically, cryogenic fluids, which are substances that exist as liquids at extremely low temperatures, have been employed in a broad variety of applications throughout industry. For example, liquid nitrogen (LN_2) is used to fast freeze food, preserve tissue and blood, and eliminate targeted tissue in cryosurgery, liquid oxygen (LOX) in life support systems and fuel cells, and liquid hydrogen (LH_2) as coolant for superconducting magnets. Recently, with interest in returning to the Moon and eventual missions to Mars and deep space, cryogenic fluids will play crucial roles in a variety of space systems, including nuclear thermal propulsion, ascent stages, descent stages, in-space fuel depots, and transfer lines that cool space experiments [10].

Cryogens feature thermal property trends that are clearly distinguishable from those of common working fluids such as wa-

---

* Corresponding author.
  E-mail address: mudawar@ecn.purdue.edu (I. Mudawar).
[1] http://engineering.purdue.edu/BTPFL

Nomenclature

c	cell size
D	channel diameter (mm)
d	distance from local cell to interface (m)
D_b	bubble diameter (m)
D_i	channel's inner diameter (mm)
D_o	channel's outer diameter (mm)
E	energy per unit mass (J/kg)
F	force per cell volume (N/m^3)
F_C	volumetric bubble collision dispersion force (N/m^3)
F_{st}	surface tension force per unit volume (N/m^3)
G	mass velocity (kg/m^{2}s)
g, g_e	gravitational acceleration (m/s^2)
h	enthalpy (J/kg)
h_{fg}	latent heat of vaporization (J/kg)
K	proportionality constant
k_{eff}	effective thermal conductivity (W/m•K)
L_a	adiabatic exit length of flow channel in experiment (mm)
L_h	heated length of flow channel (mm)
$\dot{m}$	volumetric mass flow rate (kg/m^3.s)
$\vec{n}$	interface normal vector
p	pressure (MPa)
q''	heat flux (W/m^2)
R, R_i, R_o	radial dimensions of test section (mm)
r_i	mass transfer intensity factor (s^{-1})
S_h	energy source by phase change (J/m^3)
T	temperature (°C, K)
t	time (s)
u	velocity (m/s)
u_t	liquid fluctuation velocity due to bubble agitation (m/s)
u_τ	frictional velocity (m/s)
x_e	thermodynamic equilibrium quality
y	coordinate in computational domain (m)
y^+	dimensionless distance perpendicular to channel wall
z	axial coordinate in computational domain (m)

Greek symbols

α	void fraction averaged over flow area
α_{max}	dense packing limit
ε	turbulent dissipation (m^2/s^3)
κ	interface curvature
μ	dynamic viscosity (kg/m•s)
ν	kinematic viscosity (m^2/s)
ρ	density (kg/m^3)
σ	surface tension (N/m)
φ	level set function

Subscripts

cond	condensation
evap	evaporation
f	liquid
g	vapor
sat	saturation
sc	subcooling
w	heated wall

Acronyms

BCD	bubble collision dispersion
CFD	computational fluid dynamics
CHF	critical heat flux
CLSVOF	coupled level set volume of fluid
CSF	continuum surface force
DNB	departure from nucleate boiling
HTC	heat transfer coefficient
LH$_2$	liquid hydrogen
LN$_2$	liquid nitrogen
LNG	liquified natural gas
LOX	liquid oxygen
LS	level-set
ONB	onset of nucleate boiling
PCM	phase change material
UDF	user-defined function
VOF	volume of fluid

ter or conventional refrigerants, including low liquid viscosity, μ_f, low surface tension, σ, and low latent heat of vaporization, h_{fg}. These property trends are reflected in unique fluid physics and heat transfer behavior for cryogens. For example, owing to low liquid viscosity, cryogen flows are typically associated with large Reynolds numbers, causing them to be predominantly turbulent and therefore resulting in high pressure drop. In addition, because of low σ and low h_{fg}, both the onset of nucleate boiling (ONB) and critical heat flux (CHF) are instigated at low values of wall superheat. These rather unique property attributes imply fluid flow and heat transfer correlations for cryogens must be developed separately from those of other fluid classes [11,12].

The unique two-phase heat transfer characteristics of cryogens have been investigated mostly for flow in uniformly heated round tubes, with several experimental works carried out in pursuit of correlations for pressure drop, heat transfer coefficient (HTC), and CHF. Between the 1950s and 1970s, numerous cryogenic experiments were conducted by the National Aeronautics and Space Administration (NASA). For example, Lewis et al. [13] studied near-saturated flow boiling of LN$_2$ inside a tube subjected to uniform electrical wall heating and provided results for CHF. Papell [14] measured film boiling heat transfer for LN$_2$ in a heated tube. They reported HTC for vertical upflow can be up to 8 times greater than for vertical downflow because of significantly larger vapor accumulation for the latter. They also measured the inlet velocity threshold required to negate buoyancy influence on film flow boiling.

Beginning in the early 1970s, along with continued work in the United States, experimental cryogenic flow boiling work became more prevalent in both Europe and Japan. Steiner and Schlűnder [15] carried out an extensive experimental investigation of saturated flow boiling of LN$_2$ in a horizontal tube and analyzed HTC dependence on wall heat flux, flow quality, and pressure. They also formulated a new HTC correlation, which served to overcome deviations of cryogen data from correlations for conventional fluids. They compared measured CHF for horizontal flow boiling to those for pool boiling, vertical upflow, and vertical downflow. In a companion study [16], they investigated pressure drop characteristics for horizontal saturated flow boiling of LN$_2$ and demonstrated reasonable applicability of seminal pressure drop correlations. Using Steiner and Schlűnder's same experimental facility, Muller et al. [17] conducted saturated flow boiling experiments spanning broader ranges of operating conditions, which resulted in updated power coefficients for the Steiner and Schlűnder [15] HTC correlation. Muller et al. also recommended a correlation for flow boiling CHF based on a method developed by Bonn et al. [18]. Papell and Hendricks [19] conducted subcooled flow boiling experiments with LN$_2$ in pursuit of a correlation for ONB, as their goal was to avoid bubble nucleation when cooling superconducting magnets. Klimenko [20,21] pointed out the inability of seminal HTC correlations by Chen [22] and Shah [23] at predicting cryogen

data and recommended developing a separate correlation solely for cryogenic fluids. They proposed an alternative dimensionless HTC correlation having an overall accuracy of ±35%. This correlation was validated against data by the same author [21] as well as additional experiments by Klimenko et al. [14] involving different flow orientations. They reported that channel geometry and flow orientation should not affect HTC for Froude numbers exceeding 40, for which the correlation showed greatest accuracy. Shah [24] rebutted Klimenko [20] by demonstrating superior performance of his own HTC correlation for saturated flow boiling of cryogenic fluids compared to Klimenko's as well as an earlier correlation by Rohsenow [25].

With the advent of the new millennium, research in Japan focused on two-phase heat transfer for both LH_2 and LN_2 not only to cool superconducting magnets [26–28] but also for use in other industrial applications. Tatsumoto et al. [26,27] experimentally investigated subcooled flow boiling of LN_2 in both horizontal and vertical tubes over a broad range of inlet subcooling (5-37.5 K), made possible by system pressures ranging from 0.3 to 2.5 MPa. Shirai et al. [28] continued efforts to understand two-phase heat transfer characteristics of cryogens, conducting experiments with both LH_2 and LN_2, and proposed a correlation for Departure from Nucleate Boiling (DNB) type CHF.

More recently, Chinese researchers experimentally investigated flow boiling of LN_2 with particular emphasis on micro-tubes [29–34]. On the other hand, Xu et al. [35] and Fang et al. [36] focused their work on flow boiling of LN_2 in macro-tubes.

Overall, despite some successes in obtaining experimental data for cryogens, experiments using these fluids are far more complex and require special provisions to preclude radiative heat transfer from ambient [37] sources compared to ones using more conventional fluids.

1.2. Computational methods

1.2.1. Prior two-phase computational fluid dynamics (CFD) modeling

While empirical correlations remain the most popular method for predicting transport behavior in flow boiling, they suffer the inherent weakness of being valid to specific working fluids, operating conditions, and geometries, all dictated by the database(s) from which a correlation is developed. This weakness is a primary impetus for the recent shift to more generalized CFD predictive methods.

Despite remarkable successes of CFD in predicting single-phase fluid flow and heat transfer, evidenced by good agreement with experimental data for a broad variety of flow configurations, the same cannot be said about two-phase transport. The most crucial obstacles to achieving similar successes with two-phase transport are (1) lack of robust and accurate interface tracking models, (2) lack of consensus over the commonly agreed or the most suitable numerical schemes and sub-models to implement in CFD simulations, (3) lack of 'complete' experimental validation data, including not only heat transfer data (heat flux, wall temperatures, etc.) but also detailed interfacial behavior (dominant flow pattern, local void fraction, etc.), and (4) both high computational cost and slow execution speed.

Several investigators have explored methods to enhance the applicability of CFD to two-phase situations for conventional fluids including water, refrigerants, and dielectric fluids. Lee et al. [38] constructed and experimentally validated a CFD model for flow condensation of FC-72 in a circular tube, which included a phase change sub-model, numerical discretizing methods, and convergence criteria. Kharangate and Mudawar [39] emphasized the importance of full-scale simulation of flow boiling but pointed out the majority of published CFD studies were focused on rather simple configurations such as pool boiling and single droplet dynam-

ics. Recently, Lee et al. [28–31] conducted a series of full-scale simulations of flow boiling of dielectric fluid in a partially heated rectangular channel, and validated predictions against data measured in both terrestrial gravity and microgravity.

However, when it comes to cryogenic fluids, the number of computational efforts has been quite miniscule as indicated in Table 1. Ahammad et al. [43] simulated film boiling of LN_2 and liquified natural gas (LNG) by employing Rayleigh-Taylor instability and using the volume of fluid (VOF) method for a small-scale domain comprising 12,288 cells to estimate the vapor generation rate during an accidental spill from an LNG storage tank. Zhang and Jia [44] investigated flow pattern development along a heated micro-channel by simulating bubble nucleation from a single artificial cavity using the Coupled Level Set Volume of Fluid (CLSVOF) method. Kumar and Das [45] simulated LN_2 film boiling on solid surfaces using the VOF method, validating predictions for key bubble dynamics parameters, including bubble diameter, departure frequency, and average heat flux for a range of wall superheats. Other researchers [46–48] simulated flow boiling in microchannels using the two-fluid model, a two-equation model capable of distinguishing velocities of the two phases. Despite the advantage of ability to account for velocity differences, the two-fluid model is limited by the inability to track interface topology in two-phase flows.

Overall, previous computational studies on cryogenic fluids were focused mostly on confined domains and localized two-phase phenomena. Lacking thus far have been efforts to model more realistic macro-scale flow boiling situations involving growth, coalescence, and/or breakup of large numbers of bubbles.

1.2.2. Limitations of multiphase models

As shown in Table 1, VOF has been the most popular for simulating flow boiling of cryogenic fluids. However, despite its notable advantages in ability to capture two-phase interfaces and comparatively low computing time and cost, the accuracy of VOF is compromised by use of a single momentum equation for both phases. Its inability to distinguish velocities of individual phases poses several important limitations, including: (1) streamlines penetrating the vapor-liquid interface as shown in Fig. 1(a), (2) because of the streamline penetration, the pressure field around the interface cannot be accurately predicted (which causes inaccurate prediction of relative motion between vapor and liquid [42]), and (3) because of inaccurate prediction of relative motion, abnormal bubble accumulation causes premature prediction of flow boiling CHF as shown in Fig. 1(b).

Streamline penetration across the gas-liquid interface was reported in numerous studies using VOF. Wei et al. [49] employed VOF to simulate subcooled flow boiling of water inside of a swinging flow channel. They presented predicted flow visualization results capturing nucleating bubble interfaces along the heating surface. They also presented velocity vectors superimposed with the flow visualization results, which showed clear penetration across interfaces between liquid and vapor. The penetrating velocity streamlines produced distortions to the pressure field in cells surrounding the gas-liquid interface, which in turn influenced the velocity vector of the fluid mixture. Yang et al. [50] also used VOF to investigate flow boiling of R134b inside a coiled tube. Like Wei et al., they showed velocity vectors penetrating the vapor-liquid interfaces. Similar outcomes were also witnessed by Zhuan and Wang [51] in their investigation of flow boiling of refrigerants along a circular micro-channel. As explained earlier, streamline penetration of interfaces is rooted in VOF's use of a single momentum equation. This shortcoming compromises prediction accuracy of both pressure and velocity fields around interfaces and, in turn, relative motion between the phases during bubble sliding, detachment, collision, and coalescence. Another shortcoming

Table 1
Summary of computational literature with cryogenic fluids.

Authors	Year	Fluid	Multiphase model	Pressure discretization	Application/Configuration
Ahammad et al. [43]	2016	LN_2/LNG	VOF	PRESTO	• Film boiling for risk assessment of cryogenic spill • Confined domain considering Taylor instability wavelength • 12,288 cells
Sagar et al. [70]	2021	LN_2	VOF	Body force weighted	• Pulsating heat pipe for superconductors • Microchannel ($D = 1.9$ mm) • Limited to laminar flow • 14,496 cells
Kumar and Das [45]	2022	LN_2	VOF	PRESTO	• Film boiling at solid and liquid contact plane • Confined domain only for single or multiple bubble nucleation • 12,288 cells
Zhang and Jia [44]	2016	LN_2	CLSVOF	N/A	• Microchannel flow boiling with artificially created nucleation cavity • Microchannel ($D = 1.46$ mm) • Focused on single cavity bubble nucleation • 1,023,000 cells
Zheng et al. [71]	2019	LN_2/LH_2	CLSVOF	N/A	• Horizontal chilldown process • Circular microchannel ($D = 200$ mm) • 138,240 cells
Umemura et al. [72]	2019	LH_2	CIP-LSM	N/A	• Vertical chilldown process • Circular macrochannel ($D = 12.7$ mm)
Shao et al. [47]	2016	LN_2	Two-fluid model	N/A	• Flow boiling in uniformly heated tube • Mini-channel ($D = 5$ mm) • No flow contour capturing interfacial topology • 27,750 cells
Gubaidullin and Snigerev [46]	2020	LN_2	Two-fluid model	N/A	• Flow boiling in uniformly heated tube • Mini-channel ($D = 6$ mm) • No flow contour capturing interfacial topology • 16,000 cells
Zhu et al. [48]	2020	LN_2	Two-fluid model	Body force weighted	• Natural circulation boiling • Annular macro-channel ($D_i = 70$ mm, $D_o = 120$ mm) • No flow contour capturing interfacial topology • 177,000 cells

of VOF is difficulty accurately computing local curvature from volume fractions because of sharp transition of volume fraction in vicinity of the interface. This leads to erroneous determination of local curvature and therefore compromises overall accuracy of interface topology calculations.

But, despite these shortcomings, VOF has been favored over other models because of its ability to capture interface advection without violating mass conservation [52] and comparatively highly efficient computations for large-scale domains. These merits help explain this model's popularity in flow boiling simulations.

Another popular multiphase model, the level-set (LS) model, offers the advantage of high-resolution interface reconstruction using a simple and accurate local curvature calculation method adopting a *level set function*. However, compared to VOF, the LS model suffers from larger numerical error where the interface undergoes severe stretching or tearing which, in turn, results in violation of mass conservation across the interface. This shortcoming renders its application to flow boiling situations with a large fluid domain (such as in the present study) quite elusive.

1.2.3. Strategies to mitigate limitations of VOF

Several methods have been proposed to mitigate shortcomings of both the VOF and LS models. Sussman and Puckett [53,54] developed an algorithm combining advantages of the VOF and LS models. Their 'hybrid' model employs LS to acquire accurate spatial gradient calculations at the interface and VOF for its mass conservation capability. In effect, this so-called Coupled Level Set VOF (CLSVOF) model, with its more accurate calculation of surface tension force, improves tracking of sharp interfaces (as the LS model), while also capitalizing on VOF's attribute of accurate interfacial mass conservation, ensuring less than 1% mass loss compared to up to 20% with LS [53]. Lorenzini and Joshi [52] compared simulations using the VOF and CLSVOF for flow boiling in silicon microgaps and reported superiority of CLSVOF in terms of interfacial tracking, evidenced by sharper interface reconstruction than VOF.

During the past few years, VOF has been used to model a variety of multi-phase configurations, several of which pointed to fundamental limitations of this model. One such limit, which is particularly of concern in flow boiling situations, is inability to accurately capture crucial aspects of bubble motion, including departure, dispersion, and entrainment in the bulk liquid, all of which stem from the inability to distinguish velocity differences between phases because of VOF's use of a single momentum equation. And, in systems involving impingement of liquid droplets on solid surfaces, predictions of the three-phase contact line region are compromised in the absence of accurate surface tension and dynamic contact angle models [55]. Another example is thermal energy storage using phase change materials (PCMs), where lack of accurate modeling of varying permeability and porosity compromise accuracy in mushy region velocity predictions [56].

To overcome these limitations of VOF, additional forces are incorporated as source terms in the momentum equation to mitigate under-represented relative motion between phases. Lee at al. [41,42,57] incorporated *shear-lift force*, derived from Mei and Klausner [58,59], as a momentum source term to improve prediction of bubble detachment in subcooled flow boiling of FC-72. They showed inclusion of shear lift force prevents premature prediction of CHF by providing more realistic bubble departure behavior and increasing heat transfer efficiency. Malgarinos et al. [55] proposed a model for *wetting force* which they included as momentum source term to better account for adhesive behavior of a liquid droplet impacting a heated solid surface. Their wetting force model was applied only to interface cells defined as having volume fraction value between 0.05 and 0.95. By accurately capturing dynamic changes in contact angle, this wetting force model improved prediction of maximum droplet spread along the surface.
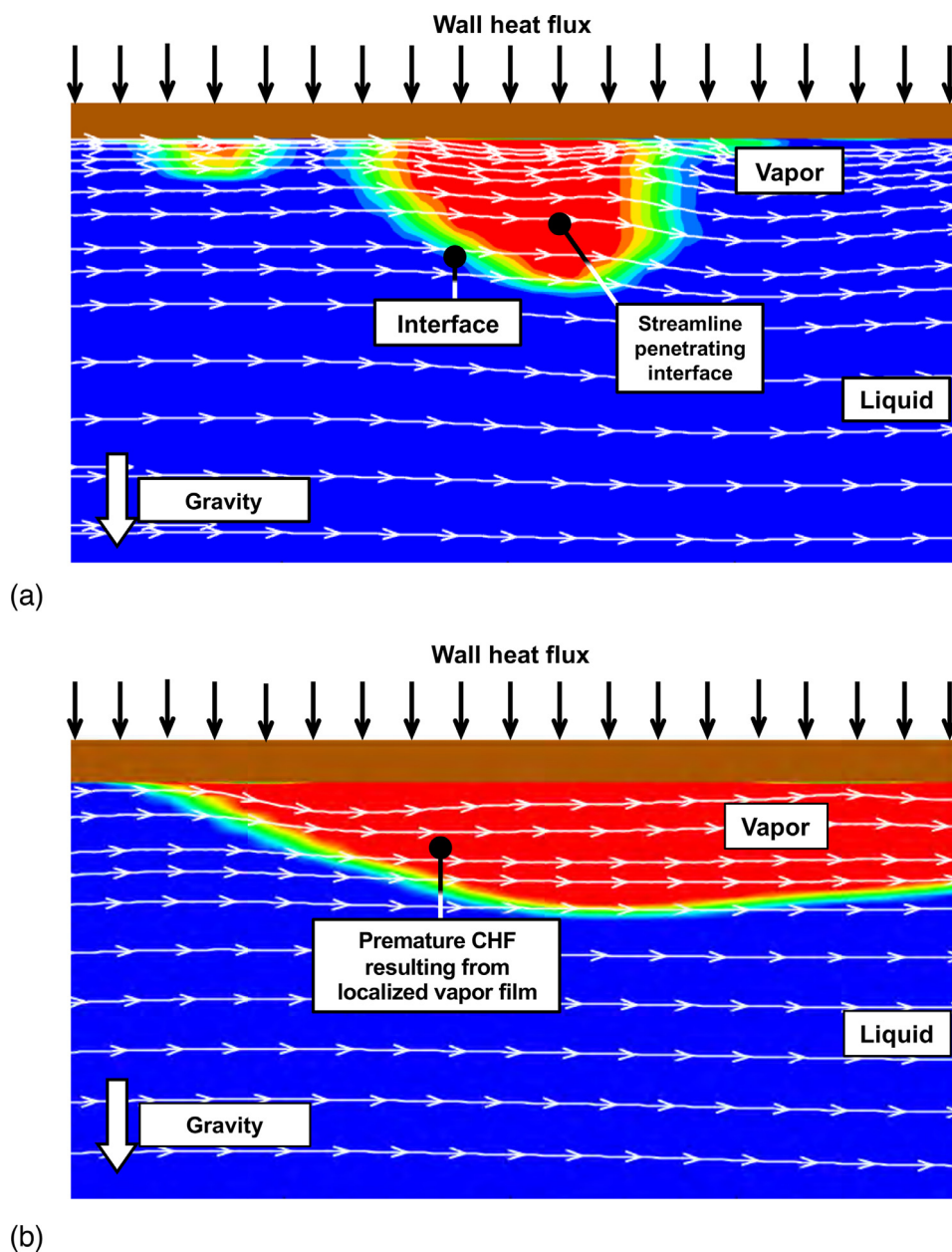
Fig. 1. Limitations of VOF model. (a) Streamline penetration of liquid-vapor interface. (b) Premature prediction of CHF.

Vogel and Thess [56] employed a momentum source term developed by Voller and Prakash [60] to actively modify fluid velocity in the mushy region where porosity and permeability greatly affect PCM behavior.

1.3. Objectives of present study

The present paper will investigate the performance of 2-D axisymmetric computational fluid dynamics (CFD) in prediction of boiling characteristics of liquid nitrogen flowing vertically upwards along a uniformly heated circular tube. Several methods will be adopted to overcome limitations of conventional multiphase CFD models employing VOF, most important of which is reliance on the more advanced CLSVOF to capture interfacial dynamics and topology more accurately, including bubble nucleation, growth, detachment, coalescence, and breakup. Further enhancement of model capability is achieved with inclusion of a *bubble collision dispersion force*, which is implemented in ANSYS FLUENT using a user-

defined-function (UDF) to overcome under-represented dispersion effects caused by bubble-to-bubble collision. A key innovation with the computing method adopted in the present study is ability to circumvent this fundamental weakness of VOF by accounting for important effects of bubble collision dispersion force in addition to utilizing CLSVOF. The combination of CLSVOF and bubble collision dispersion force has not been attempted before for flow boiling simulations.

Key objectives of this study are to:

(1) Develop UDF for bubble collision dispersion force which is implemented in a two-phase computational model that overcomes innate shortcomings of VOF.

(2) Validate predictions of the new model against data from prior benchmark experiments.

(3) Utilize high resolution CFD predictions to investigate axial variations of interfacial flow pattern, fluid temperature, and fluid velocity, flow characteristics that are very difficult to measure in cryogenic experiments.

2. Computational methods

2.1. Mathematical representation and numerical details

In the present study, a 2-D axisymmetric transient Coupled Level Set Volume of Fluid (CLSVOF) approach is implemented in ANSYS FLUENT, taking advantage of its improved tracking of interfacial topology (compared to VOF) during cryogenic flow boiling in a uniformly heated vertical circular tube.

2.1.1. Governing equations

As indicated in Eqs. (1) and (2) below, mass conservation for each phase is expressed in terms of temporal variation and advection of corresponding volume fraction for each phase balanced by net mass transfer in and out of each cell via phase change,

$$\frac{\partial \alpha_f}{\partial t} + \nabla \cdot \left(\alpha_f \vec{u_f} \right) = \frac{1}{\rho_f} \sum (\dot{m}_{gf} - \dot{m}_{fg}) \tag{1}$$

$$\frac{\partial \alpha_g}{\partial t} + \nabla \cdot \left(\alpha_g \vec{u_g} \right) = \frac{1}{\rho_g} \sum (\dot{m}_{fg} - \dot{m}_{gf}) \tag{2}$$

where α, $\vec{u}$, $\dot{m}$, and ρ are volume fraction, velocity, mass flow rate per cell volume, and density, respectively, and subscripts f and g represent liquid and vapor, respectively.

The most distinctive feature of CLSVOF is inclusion of surface tension force in the momentum equation. Like VOF, CLSVOF involves solving a single mixture momentum equation using pseudo-mixture properties,

$$\frac{\partial (\rho \vec{u})}{\partial t} + \nabla \cdot (\rho \vec{u} \vec{u}) = -\nabla p + \nabla \cdot \mu \left[\nabla \vec{u} + (\vec{u})^T \right]$$
$$- \sigma \kappa \delta(\varphi) \nabla \varphi + \rho \vec{g} + F^{BCD} \tag{3}$$

where σ, κ, φ are surface tension, interface curvature, and level set function, respectively. Details concerning fluid property formulations are identical to those in VOF, which are available from ANSYS [61] and therefore, for purpose of brevity, will not be explained in this paper.

Energy conservation in CLSVOF model is identical to that in VOF and is given by

$$\frac{\partial (\rho E)}{\partial t} + \nabla \cdot (\vec{u}(\rho E + p)) = -\nabla \cdot (k_{eff} \nabla T) + S_h \tag{4}$$

where S_h is an energy source term describing latent heat transfer via phase change.

$$S_h = \dot{m}_{fg} h_{fg} \tag{5}$$

Interfacial mass transfer is modeled according to the Lee model [62]

$$\begin{cases} \dot{m}_{fg} = r_{i,evap} \alpha_f \rho_f \frac{(T_f - T_{sat})}{T_{sat}} & \text{for evaporation} \\ \dot{m}_{gf} = r_{i,cond} \alpha_g \rho_g \frac{(T_{sat} - T_g)}{T_{sat}} & \text{for condensation} \end{cases} \tag{6}$$

wherein $r_{i,evap}$ and $r_{i,cond}$ are empirical *mass transfer intensity factors* having unit of s^{-1}. Lee et al. [38] reviewed a wide range of computational phase change studies and noted that values for these factors must be tailored to specifics of flow configuration, geometry, mesh, and even time step size. In general, excessively high values can pose numerical convergence issues, whereas very small values can result in appreciable discrepancy between interfacial and saturation temperatures.

Recently, Yeo and Lee [63] investigated previous flow boiling computational studies that utilized the Lee model [62] and showed that r_i values employed in a variety of flow boiling configurations varied between 0.1 and 1000 depending on system geometry, working fluid, and operating conditions. Unfortunately, it is very
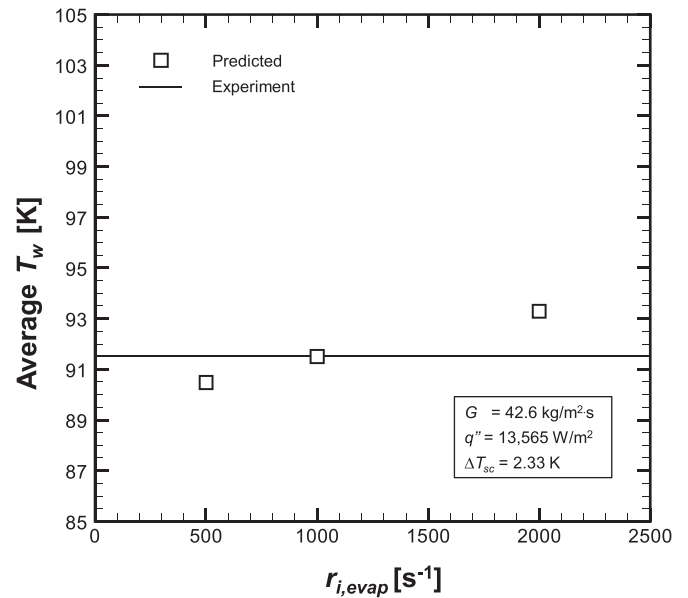

Fig. 2. Comparison of predicted and measured average wall temperatures for three different values of $r_{i,evap}$.

difficult to recommend r_i values for cryogenic flow boiling situations a priori from previous literature. Therefore, values of $r_{i,evap}$ ranging from 500 to 2000 are tested in the present study for flow boiling of LN_2 (details of the experimental validation will be discussed in a later section). Note that the present study is focused on near-saturated inlet conditions where bulk liquid temperature is close to saturation over most of the fluid domain. Therefore, condensation effects during flow boiling, such as bubble recondensation in liquid core, are miniscule compared to situations involving highly subcooled inlet conditions. This explains reasons behind investigating effects of variable $r_{i,evap}$ while keeping $r_{i,cond}$ anchored at 100. Fig. 2 shows average wall temperature predictions for three different $r_{i,evap}$ values compared to measured average wall temperatures. Notice how predicted temperature increases monotonically with increasing $r_{i,evap}$, with the intermediate value of $r_{i,evap} = 1000$ yielding best agreement with experiment. Therefore, values used in this paper are $r_{i,evap} = 1000$ and $r_{i,cond} = 100$.

It must be noted that, unlike VOF, using CLSVOF within ANSYS FLUENT, interfacial mass transfer terms in the mass and energy conservation equations are computed via user-defined functions (UDFs) as source terms for each phase.

2.1.2. Interface topography representation using CLSVOF

Ability of CLSVOF to provide more accurate interface topology is key to accurate simulation of surface tension force which, in turn, enhances accuracy in predicting overall force balance on individual bubbles and therefore more accurate prediction of the bubble formation cycle from nucleation to detachment.

As indicated in Eq. (7), the *level set function*, φ, used in CLSVOF is defined as a signed distance d to the interface, positive for primary (liquid) phase and negative for secondary (vapor) phase, with the interface designated as $\varphi = 0$.

$$\varphi(x, t) = \begin{cases} +|d| & \text{if } x \text{ belongs to primary phase} \\ 0 & \text{if } x \text{ belongs to interface} \\ -|d| & \text{if } x \text{ belongs to secondary phase} \end{cases} \tag{7}$$

This formulation renders the level set function smooth and continuous across the interface. In CLSVOF, interface normal vector, $\vec{n}$, and curvature, κ, are calculated, respectively, according

to

$$\vec{n} = \frac{\nabla\varphi}{|\nabla\varphi|}\Big|_{\varphi=0} \tag{8}$$

$$\kappa = \nabla \cdot \frac{\nabla\varphi}{|\nabla\varphi|}\Big|_{\varphi=0} \tag{9}$$

This formulation represents a fundamental advantage over VOF, where the calculation of interface normal vector and curvature relies on spatial derivative of volume fraction, which is intrinsically discontinuous across the interface, resulting in compromised representation of the interface [61]. With reliance on the smooth and continuous level set function across the interface, CLSVOF enables accurate calculation of surface tension force and therefore more accurate capture and simulation of small bubble dynamics, fluid motion, and heat transfer. In the present CLSVOF formulation, calculation of surface tension is based on *Continuum Surface Force* (CSF) model proposed by Brackbill et al. [64],

$$F_{st} = \sigma \frac{\rho\kappa\delta(\varphi)}{0.5(\rho_f + \rho_g)} \tag{10}$$

where F_{st} is a volumetric surface tension force, and function $\delta(\varphi)$ is given by

$$\delta(\varphi) = \begin{cases} \frac{1+\cos\left(\frac{\pi\varphi}{a}\right)}{2a} & if \ |\varphi| < 0 \\ 0 & if \ |\varphi| \geq 0 \end{cases} \tag{11}$$

where in $a = 1.5h$, h being the grid spacing of local mesh.

Advection and evolution of level set function are calculated according to

$$\frac{\partial\varphi}{\partial t} + \nabla \cdot (\vec{u}\varphi) = 0 \tag{12}$$

in a manner similar to that of VOF. Note, however, that Eq. (12) is used to model advection and devolution of the level set function and not mass conservation. In CLSVOF, mass conservation is modeled in terms of volume fraction in accordance with Eqs. (1) and (2).

2.2. Bubble collision dispersion force

As discussed in the introduction, relative interfacial motion generated by different phase velocities is under-represented in single-equation models, including both VOF and CLSVOF. To correct this shortcoming and improve the present CLSVOF model's ability to more accurately predict bubble growth and detachment, which are both kernel for flow boiling simulations, an additional term which accounts for *Bubble Collision Dispersion (BCD) force* is included in the momentum conservation equation as a source term. Sharma et al. [65] introduced the following relation for BCD force per unit volume of mixture,

$$F^{BCD} = -\left(K\frac{\rho_f u_t^2}{2\alpha_{g,max}^{2/3}}\right)f(\alpha_g)\nabla\alpha \tag{13}$$

where α_{max} and K are *dense packing limit* and proportionality constant, with recommended values for bubbly flow of 0.62 and 1, respectively, and α_g is void fraction. Also included in Eq. (13) are liquid fluctuation velocity, u_t, resulting from liquid agitation, which accounts for turbulent intensity effects on bubble dispersion, and function $f(\alpha_g)$, defined as

$$f(\alpha_g) = \alpha_g^{2/3}\left[1 - \left(\frac{\alpha_g}{\alpha_{g,max}}\right)\right] \tag{14}$$

From Eq. (13), determining the magnitude of BCD force requires predetermination of liquid fluctuation velocity, u_t which has
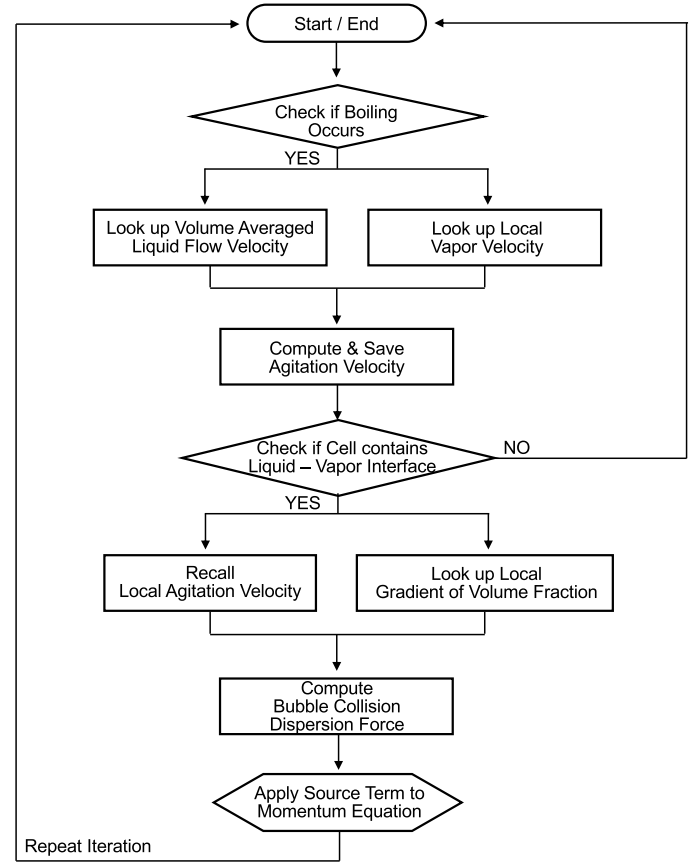

Fig. 3. Flow chart for UDF used to compute bubble collision dispersion force.

been modeled with turbulent dissipation and bubble diameter in Sharma et al. [65]. Unfortunately, it is both computationally complex and expensive to determine u_t around every bubble along the heated wall of a channel since bubble size, shape, and motion, and therefore bubble-induced liquid turbulence, all vary with space and time. In the present near-saturated flow boiling configuration (described in a subsequent section), detached vapor bubbles change shape and size due to both bubble-induced turbulence and condensation, which affects both interfacial forces and bubble virtual mass. As each bubble deforms in anisotropic fashion during the flow boiling process, it is extremely difficult to determine the exact magnitude of local fluctuating velocity along the bubble interface. Because of these complicating factors, the present study defines u_t as the net velocity difference between the average velocity of liquid flow and vapor phase velocity at each cell,

$$u_t = (\varepsilon D_b)^{1/3} \approx |\bar{u} - u_{local}| \tag{15}$$

values of which are updated every iteration.

Appling the BCD force formulation in the present simulations is achieved with aid of an algorithm that is coded via a user-defined function (UDF). Fig. 3 shows a flow chart detailing application of this algorithm to calculate the BCD force. For situations where the fluid enters the channel in subcooled liquid state, bubble collision dispersion force plays no role in the inlet region. Once phase change takes effect, the algorithm identifies cells occupied only by liquid phase whose volume fraction equals exactly zero and loops around all the liquid only cells to calculate area mean liquid velocity and return the calculated value every numerical iteration. Agitation velocity for each cell is then calculated as difference between mean liquid velocity and local velocity of fluid in accordance with Eq. (15). The agitation velocity is then saved into allocated

Table 2
Summary of grid independence test.

	Case a	Case b	Case c	Case d
Grid size	4 μm	6 μm	10 μm	20 μm
Radial direction mesh	280	250	200	100
Axial direction mesh	2500	2500	2500	2500
Converged average T_w	91.52	91.70	92.19	93.94

memory and recalled when needed. The algorithm then detects vapor-liquid interfaces by identifying cells having volume fraction greater than zero and less than unity. At the identified cells, the saved agitation velocity are recalled and used to calculate volume fraction and gradient of volume fraction for each cell, and hence BCD force, according to Eq. (13). The calculated BCD force is then applied as a source term in the momentum conservation equation for cells containing interfaces.

2.3. Computational domain and grid independence test

Fig. 4 details the computational domain employed in this study. The domain simulates actual test section geometry from benchmark experiments described in detail in a later section. The domain is a two-dimensional axisymmetric center cut surface of a cylindrical tube having inner radius of 7.05 mm, heated length of 410 mm, and additional adiabatic length of 60 mm, the latter intended to prevent unwanted exit effects. The inlet chamber geometry is also included in the computational domain to accurately capture hydrodynamic effects of sudden expansion into the inlet chamber. The fluid domain is divided into two sections, one encompassing the heated portion and the other the adiabatic portion. The computational domain includes a solid zone of 0.9-mm thick stainless steel, mimicking the tube wall thickness from the actual benchmark experiments, which allows capture of conjugate heat transfer from solid to fluid. A quadrilateral mesh is applied to the entire computational domain using ANSYS ICEM. Non-uniform mesh sizes are utilized with refinement near the wall not only to accurately capture fluid-thermal interactions in the viscous sublayer but also to capture micro-nucleation happening from vapor embryos in the wall region.

Grid sensitivity is tested to ensure grid independency of the model. Four different grids are constructed with four different cell sizes near the wall as shown in Table 2. For the grid independence test, intermediate operating condition having mass velocity of 42.6 kg/m²s, heat flux of 13.6 kW/m², and inlet subcooling of 2.28 K, was selected to represent overall test conditions spanning from low to high heat flux. For each of grid size, the area averaged heated wall temperature following quasi-steady convergence is compared to experimental data. Fig. 5(a) shows asymptotic convergence of average wall temperature is achieved for near wall cell size below 6 μm. In this study, 100 μm is used for the bulk region decreasing to 4 μm near the wall.

When using a turbulence model, it is crucial to adopt an acceptably low value for non-dimensional distance from the wall, which is defined as

$$y^+ = \frac{y u^\tau}{v_f} \quad (16)$$

where y, u_τ, v_f are distance from the wall, friction velocity, and liquid kinetic viscosity, respectively. Low-Re turbulent models such as k-ω SST, which is adopted in the present simulations, aim to resolve the viscous sublayer, and therefore require that y^+ be smaller than thickness of the laminar sublayer of $y^+ = 5$. This is also important when simulating flow boiling situations like the present, where capturing heat transfer interactions in the viscous sublayer
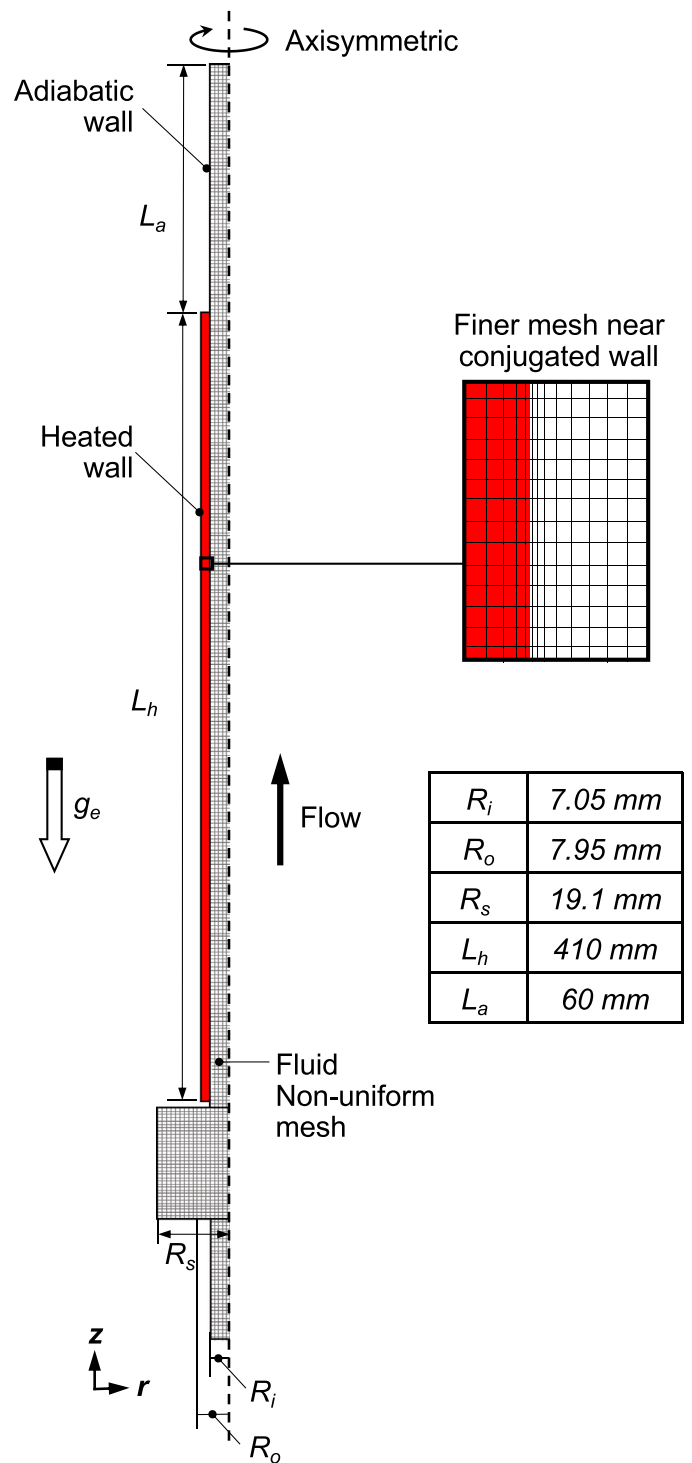

Fig. 4. Schematics of computational domain and mesh grid.

R_i	7.05 mm
R_o	7.95 mm
R_s	19.1 mm
L_h	410 mm
L_a	60 mm

is vital to accurate prediction of bubble initiation and growth. As shown in Fig. 5(b), with the selected grid, wall y^+ values are below 5 along the entire heated length, satisfying the highlighted requirement.

2.4. Initial and boundary conditions

In this study, four different LN$_2$ flow boiling cases are simulated as indicated in Table 3, mimicking actual test conditions. Note that pre-calculated fully developed velocity profiles corresponding to
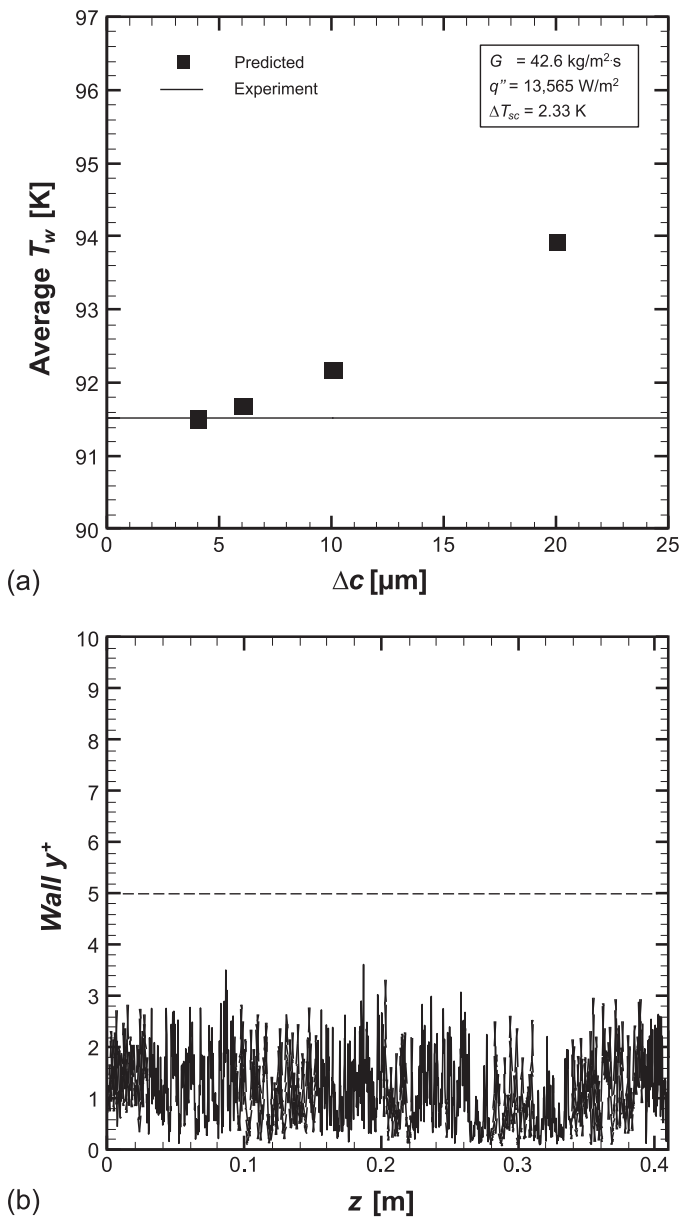
Fig. 5. (a) Effects of near-wall grid size on predicted average wall temperature. (b) Variation of non-dimensional distance from the wall along heated length for selected grid size.

Table 3
Operating conditions of present simulations.

	Fluid	Mass velocity [kg/m².s]	Inlet Pressure [MPa]	Wall heat flux [W/m²]	Inlet subcooling [K]
Case 1	LN₂	43.9	0.34	7,413	2.33
Case 2	LN₂	42.6	0.34	13,565	2.28
Case 3	LN₂	42.3	0.34	20,505	2.28
Case 4	LN₂	43	0.34	32,808	2.28

each mass velocity (G = 42.6, 42.3, 43, 42.2 kg/m².s) and accompanying turbulent properties are applied at the fluid domain's inlet as boundary conditions. A no-slip condition is applied to all wall boundaries. In CLSVOF, wall adhesion angle, which influences surface normal and curvature in cells near the wall, is specified via the surface tension model used. In this study, the wall adhesion angle between vapor-solid interface and vapor-liquid inter-

face is specified at 172.5° for LN_2 [66]. Interfaces between solid and fluid domains are applied with a coupled heat flux condition to capture conjugate heat transfer. Inlet velocity and outlet pressure are adopted, respectively, as inlet and outlet boundary conditions. Table 4 provides LN_2 property values used in the simulations, which are saturation values based on measured system pressure (only one pressure value is provided from experiment). For all four test cases, liquid initially fully occupies the entire domain with fully developed velocity corresponding to each mass velocity case. Numerical stability is maintained by employing a global Courant number of 0.7 and using variable time-step ranging from 10^{-5} to 10^{-9} s. Table 5 provides details of the numerical scheme adopted in the computations.

3. Benchmark experimental investigation

3.1. Experimental setup and test conditions

Experiment results from Lewis et al. [13] are selected as benchmark for validating the CFD simulations. Despite being a half century old, this reference is one of the most relevant and comprehensive experimental investigations for flow boiling of LN_2 along a circular tube, providing not only tabulated experimental data but also detailed geometrical information for the test apparatus. Shown in Fig. 6, the main test section assembly is comprised of an electrically heated tube, inlet and outlet chambers, and vacuum jackets. The heated tube is made of 304 stainless steel and has inner radius of 7.05 mm, thickness of 0.889 mm, and effective heated length of 410 mm. Having an inner radius of 19.1 mm, the inlet chamber provides a buffer region by decreasing flow velocity, preventing heat leakage from the heated test section to the incoming liquid. Because of the expansion followed by contraction of the flow in the inlet chamber, hydrodynamic behavior of liquid at the heated test section inlet is different from that of fully developed flow for a plain constant diameter tube. More specifically, the contraction increases turbulence effects for the heated test section's near-wall region and further enhances convective heat transfer between wall and liquid. The ensuing axial increase of wall temperature in the inlet region of the heated test section is therefore expected to be slowed, causing delayed ONB. Wall temperatures were measured with copper-constantan thermocouples which were soldered to the outside wall of the heated tube. Additional details of the experimental setup are available in the original reference [13].

Tabulated axial wall temperatures are plotted in Fig. 7 for four different LN_2 cases that are selected for validation of the CFD predictions. Noted here is some scatter of the temperatures, brought about by use of copper-constantan thermocouples, in addition to the second thermocouple from the inlet constantly measuring higher temperatures when compared to measurements of neighboring thermocouples. For this reason, second thermocouple measurements are deemed clear outliers which need to be segregated from the temperature data considered. To validate the present CFD predictions, only wall temperature data starting from the third thermocouple are compared to predicted temperatures.

4. Results and discussion

4.1. Effects of bubble collision dispersion (BCD) force

Fig. 8 compares two different flow boiling simulation results at mass velocity of 42.6 kg/m².s, heat flux of 13565 W/m² and inlet subcooling of 2.28 K, one without inclusion of BCD force and another with. Here, it should be noted that large number of bubbles is tracked in both cases to assess the effect of the BCD force. Also, figures presented in this paper are representative of large-

Table 4
Thermophysical properties used in the simulations.

Fluid	P [MPa]	T_{sat} [K]	h_{fg} [J/kmol]	ρ_f [kg/m³]	$c_{p,f}$ [J/kg.K]	k_f [W/m.K]	μ_f [kg/m.s]	ρ_g [kg/m³]	$c_{p,g}$ [J/kgK]	k_g [W/mK]	μ_g [kg/m.s]	σ [N/m]
LN₂	0.34	89.5	5.07×10^6	748.3	2133.4	0.1211	1.05×10^{-5}	14.3	1255.4	0.0088	6.43×10^{-6}	0.0062
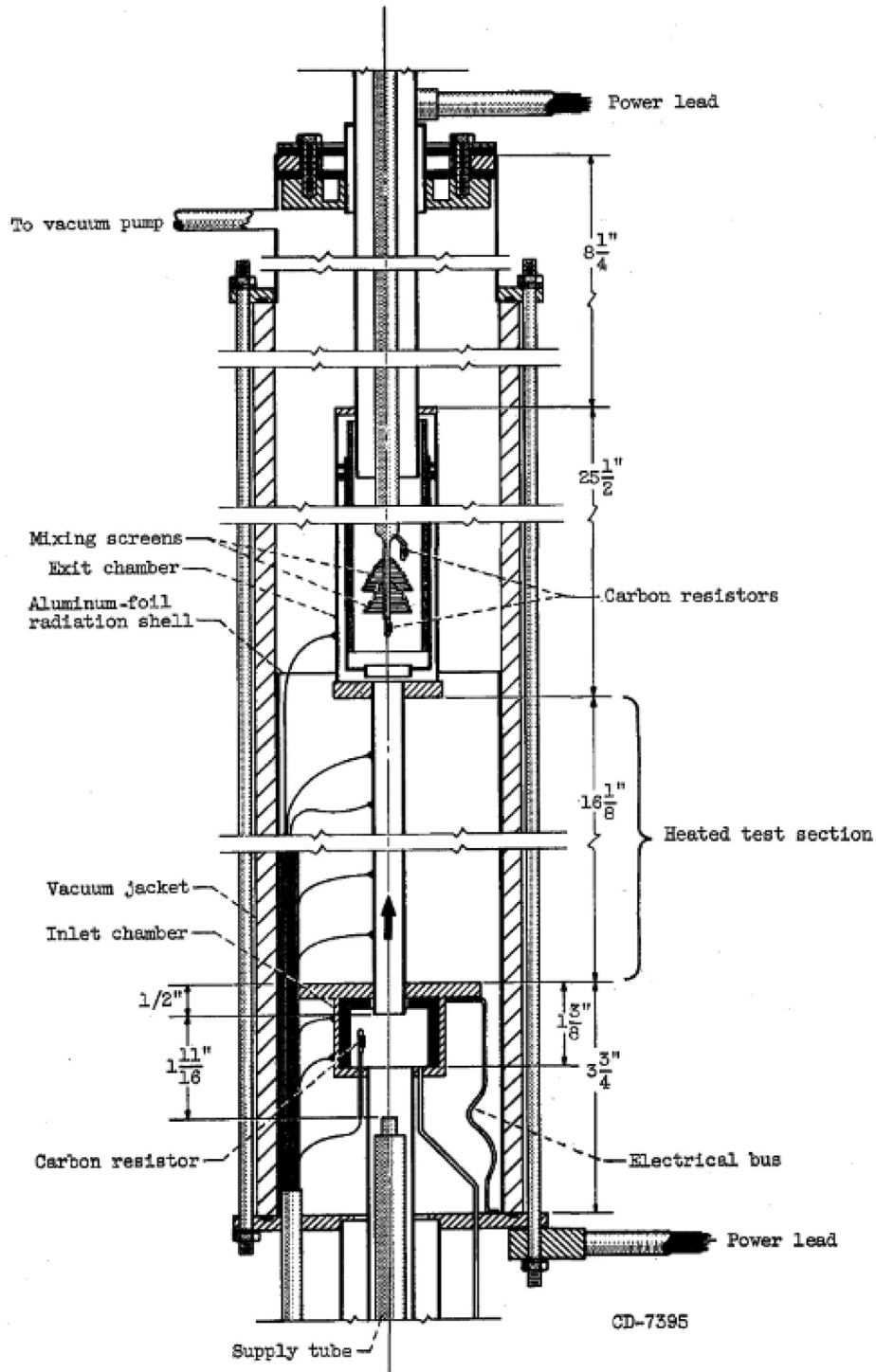
Fig. 6. Test section geometry of benchmark experimental investigation. Adapted from Lewis et al. [13].

Table 5
Discretization method used in the simulations.

Variable	Discretization method
Pressure-velocity coupling	Pressure-implicit with splitting of operators (PISO)
Gradient	Least square cell based
Pressure	Body force weighted
Momentum	Second order upwind
Volume fraction	Geo-reconstruct
Turbulent kinetic energy	First order upwind
Specific dissipation rate	First order upwind
Energy	Second order upwind
Level-set function	First order upwind
Transient formulation	First order upwind
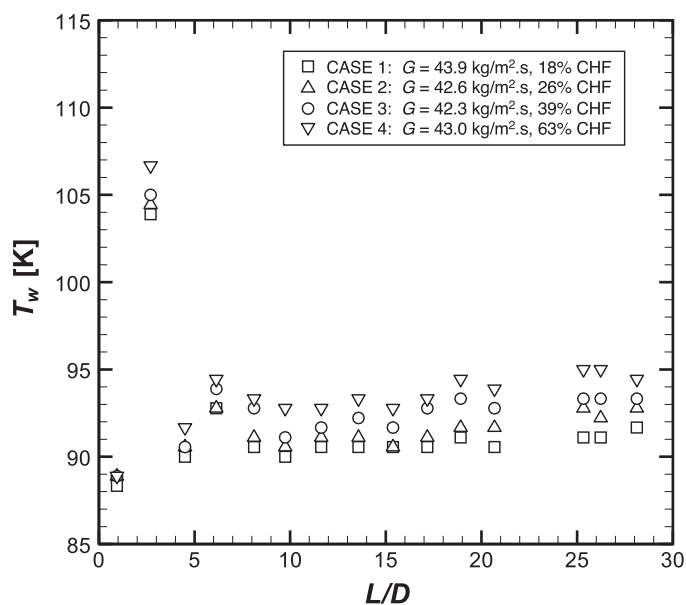
Fig. 7. Plot of wall temperature versus distance along heated tube. Adapted from Lewis et al. [13].

scale flow patterns which can clearly depict individual bubble behaviors.

Fig. 8(a) shows transient evolution of flow contours without inclusion of the BCD force for a 2-cm long heated region centered at $z = 2.5$ cm. These contours are captured with a time step of 0.01 s after reaching steady state. Colored dots indicate a target bubble to be tracked for analysis. At initial time t_0, a single bubble is flowing upwards, entrained in the core liquid flow, as another is nucleating on the heated wall. Notice how the first bubble is gradually approaching the nucleating bubble as the latter detaches from the wall. Also noticeable is how the faster first bubble from the liquid core outpaces the latter bubble, evidenced by distance between the two bubbles getting closer. After 0.08 s, the two bubbles collide because of the velocity difference and begin to merge. After 0.09 s, the two bubbles are completely coalesced into a single larger vapor bubble. This depiction of bubble trajectory and merging of bubbles following collision is observed along the entire flow channel when BCD force is not activated.

Fig. 8(b) shows transient evolution of flow contours at the mentioned operating conditions with BCD force this time included in the simulations. Predictions are shown for two axial locations, Region I and Region II, centered at $z = 3.25$ and 7.25 cm, respectively. Note that both sets of flow contours are captured at the same time and with the same time step after reaching steady state. For Region I, a single bubble is seen flowing upwards while also approaching

another bubble that has detached from the heated wall. The two bubbles approach each other reaching closest distance after 0.02 s before appearing to collide head-to-head. After the collision, the two bubbles do not coalesce but bounce away in nearly opposite flow directions and get dispersed away from one another. Note that the recorded time step size of 0.01s is not short enough to capture the precise moment of collision of the two bubbles. Similar dispersion behavior is captured in Region II for the same period. A single bubble is shown flowing upwards while also approaching a second bubble that has detached from the heated wall. After 0.02 s, the two bubbles appear to collide, this time side-to-side rather than head-to-head. Being much faster than the detached bubble, the bubble from the bulk liquid flow incurs severe distortion in its flow direction, a nearly 90-dgree turn, whereas distortion for the near-wall bubble is much weaker.

As explained, Fig. 8(a) and (b) capture in-depth progress of bubble collision and dispersion, but in Fig. 8(c), large-scale flow patterns are compared for cases with and without BCD force at two different axial locations. To the left of Fig. 8(c), flow patterns with and without BCD force for $z = 0 – 0.1$ m are provided to illustrate strong bubble dispersion resulting from BCD force in the upstream region of the heated tube. To the right of Fig. 8(c), another set of flow patterns is shown for $z = 0.15 – 0.25$ m to highlight consequential vapor structure farther downstream where vapor coalescence is intensified because of a weakening of BCD force. The middle part of Fig. 8(c) captures flow contours for the entire flow channel at steady state with and without inclusion of the BCD force. Note that both flow contours, one with BCD and the other without BCD, are provided for identical axial locations to compare the effects of BCD force under identical flow conditions. Readily apparent are smaller bubble sizes and smaller void fraction for the upstream region. In the inlet region, with BCD force, small, detached bubbles approach each other before bouncing away with virtually no coalescence. This behavior results in smaller sized bubbles in the core in the upstream region and reduced coalescence and smaller size of large coalescent bubbles in the downstream region as compared to the case without BCD force, this despite the dispersion effect being less dominant for larger bubbles. Notice, for the downstream region with inclusion of BCD force, the dispersion of small sized bubbles between and around the larger bubbles, evidence of additional bubble breakup resulting from bubble-to-bubble collisions.

Overall, the flow contours in Fig. 8 clearly capture the profound influence of BCD force on interfacial behavior along the channel, which is evident in flow pattern development and expectedly heat transfer behavior as well. In the following section, all provided results are for simulations including the BCD force.

Fig. 9(a) shows the relationship between BCD force effect and interface area to vapor volume ratio, $A_{interface}/V_{single\ bubble}$. With decreasing $A_{interface}/V_{single\ bubble}$, (i.e., increasing bubble size), the effect of BCD force on a bubble decreases. Fig. 9(b) depicts attenuated effects of BCD force on large bubbles or slugs, evidenced by increased tendency for bubble to coalesce together rather than disperse. Shown is transient evolution of flow contours, captured for indicated operating conditions with a time step of 0.01 s after reaching steady state, with BCD force for an 8-cm long heated region centered at $z = 26$ cm. Red and blue dots indicate target bubbles to be tracked for analysis. Toward the middle region of the contour, marked with red dots, a large bubble is approaching two small bubbles flowing ahead. Due to faster velocity of the larger bubble, the small bubbles are overtaken and coalesce into the larger bubble. Toward the outer region, marked by blue dots, a large bubble is shown engulfing neighboring small bubbles rising from the heated wall. Bubbles captured in both situations clearly illustrate the attenuation of BCD force effects for larger bubbles. Comparing Figs. 8(b) and 9(b), it is evident that the effect of BCD
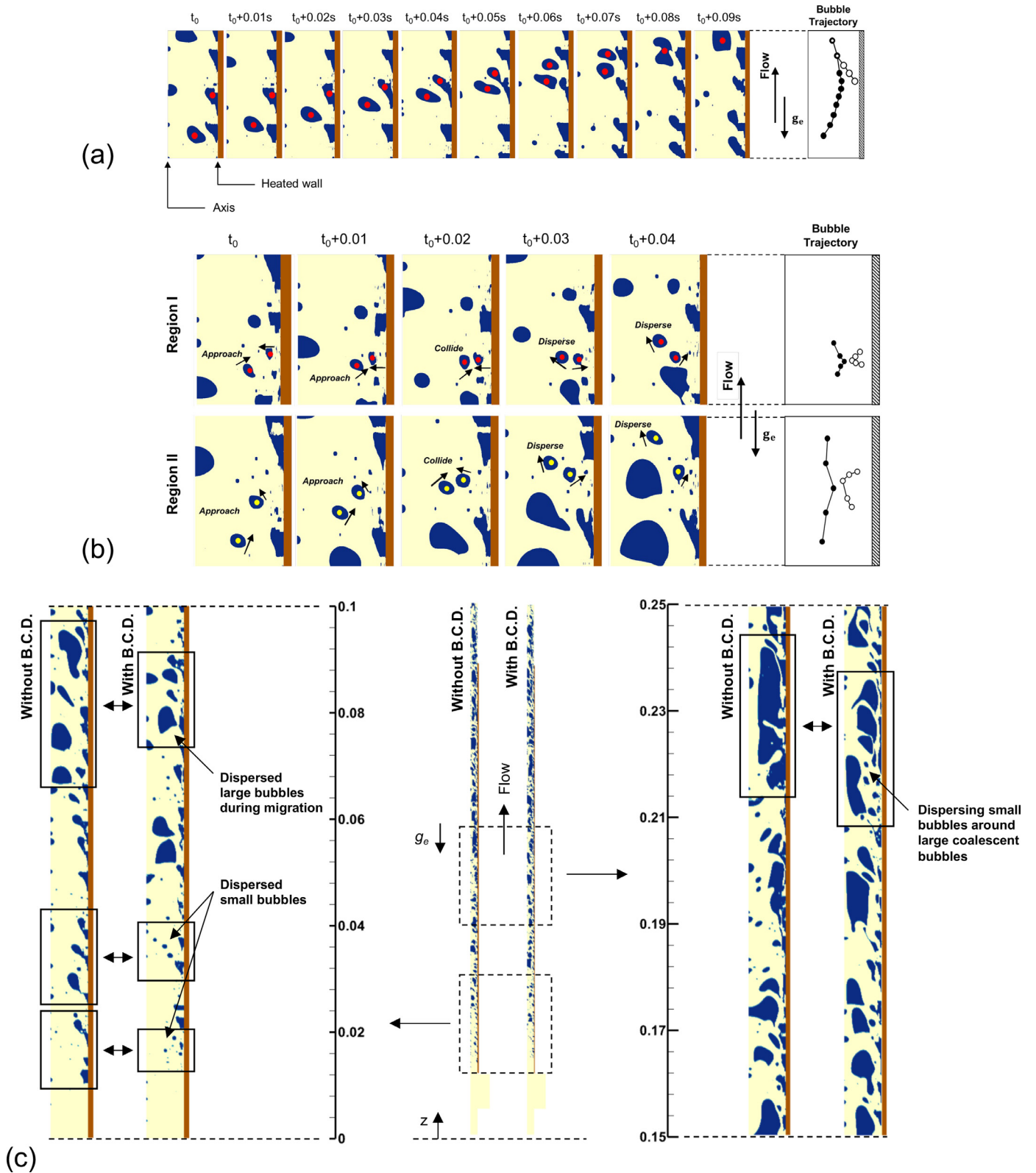
Fig. 8. (a) Transient interfacial dynamics and relative bubble motion for 2 cm long heated region centered at $z = 2.5$ cm without inclusion of bubble collision dispersion (BCD) force. (b) Transient interfacial dynamics and relative bubble motion for $z = 2.5$-4.0 cm and $z = 6.5$-8.0 cm with inclusion of BCD force. (c) Overall comparison for simulations with and without inclusion of BCD force. Operating condition for all cases shown are $G = 42.6$ kg/m².s, $q'' = 13565$ W/m², and inlet subcooling of $\Delta T_{sc} = 2.28$ K.
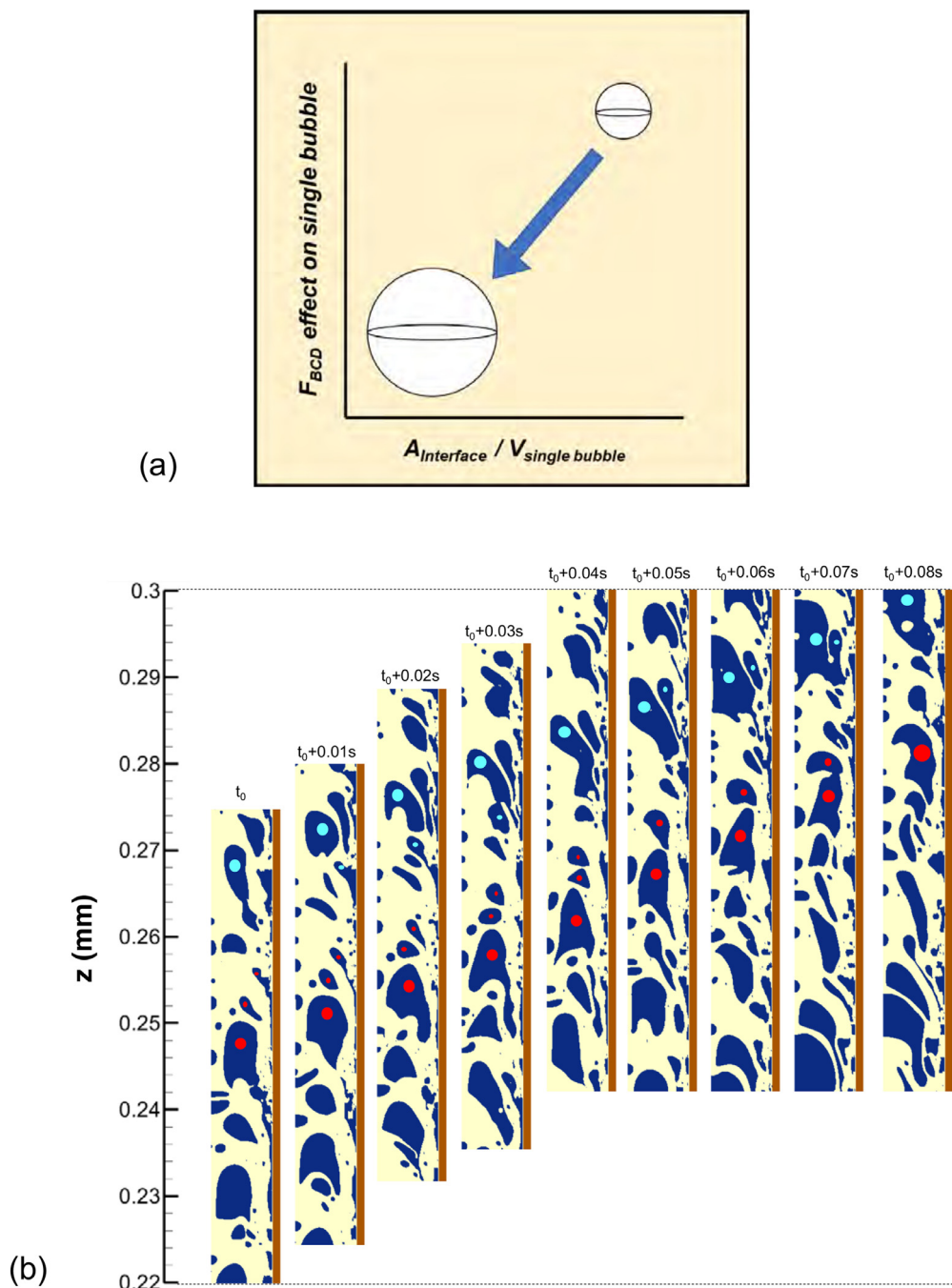
Fig. 9. (a) Schematics for relation between BCD force effect and interfacial area to single bubble volume ratio. (b) Transient interfacial dynamics for $Z = 22$ - 30 cm. Operating condition for all cases shown are $G = 42.6$ kg/m^2.s, $q'' = 13565$ W/m^2, and inlet subcooling of $\Delta T_{sc} = 2.28$ K.

force differs by the size of bubbles, culminating in different bubble behaviors.

In addition, to assess effects of BCD force more clearly, radial distributions of vapor volume fraction are compared in Fig. 10 for same operating conditions with and without inclusion of BCD force. With BCD force, bubbles disperse after colliding with each other as shown earlier in Fig. 8(b). This is reflected in Fig. 10 as flatter radial distribution of vapor volume fraction with as compared to without BCD force. Furthermore, because BCD force reduces likelihood of bubble coalescence, the magnitude of void fraction at each axial location is smaller with than without BCD force. This effect was validated by Sharma et al. [65] who utilized BCD force as a closure interfacial force in their two-fluid model. In addition, the effect of BCD force was shown by Lee et al. [67] to

enhance predictive accuracy in horizontal flow boiling simulations even when using the conventional VOF model.

4.2. Flow visualization results

4.2.1. Flow regime predictions

Fig. 11 shows computational flow contour results using CLSVOF, BCD force included, captured after reaching steady state. Shown are contours of LN$_2$ flow boiling along the entire heated length as well as the additional adiabatic length downstream of the test section for vertical upflow boiling with near saturated inlet conditions and heat fluxes of $q'' = 7413$, 13565, 20505, and 32808 W/m^2. Mass fluxes for the four cases are different but all within a very narrow range of 42.3 – 43.0 kg/m^2.s.
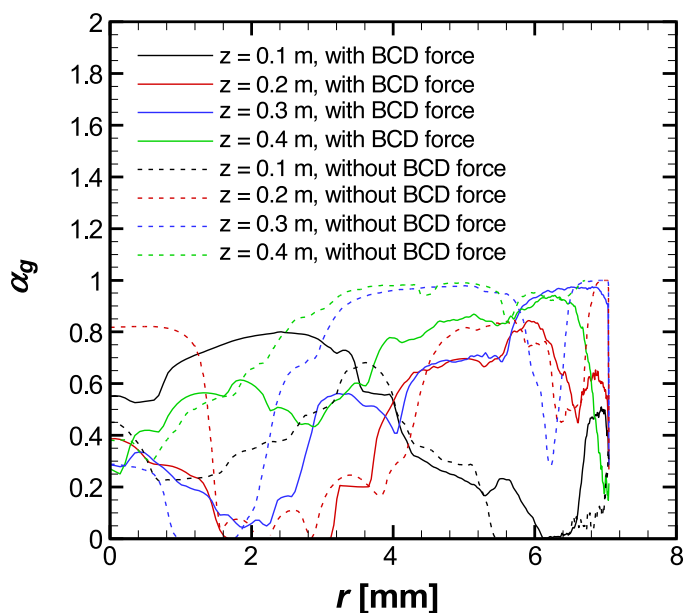
Fig. 10. Comparison of radial volume fraction profiles at four different axial locations for simulations with and without inclusion of BCD force. Operating conditions are $G = 42.6$ kg/m^2.s, $q'' = 13,565$ W/m^2, and inlet subcooling of $\Delta T_{sc} = 2.28$ K.

With the small amount of inlet subcooling, pure liquid enters the heated section and tiny bubbles begin nucleating in the upstream region once sufficient wall superheat is acquired. The nucleated bubbles grow in size as they move in the axial direction and begin to detach from the heated wall and migrate towards the channel core. Notice the "necking phenomenon" captured in Fig. 11(a) and (b), prevalently in the upstream near wall region where larger detaching bubbles leave small vapor residue at the heated wall which initiates another cycle of growth to detachment farther downstream. The detached bubbles are exposed to higher core liquid velocity, causing them to move faster and engulf surrounding slower smaller bubbles, culminating in larger coalescent oblong bubbles along the core. It should be noted that *BCD effect is no longer dominant for large bubbles as interface area per vapor volume decreases appreciably thereby reducing BCD force*. Therefore, with the abating BCD effect, appreciably grown bubbles begin to merge and coalesce, forming even larger oblong vapor bubbles and triggering flow regime transition from bubbly to churn-slug. The oblong bubbles grow even longer along the flow direction with continued coalescence. Additional tiny bubbles are captured around the large oblong bubbles due to vapor pinching and bubble breakup resulting from velocity difference between fast moving large bubbles and surrounding liquid.

Clear differences are noticed in Fig. 11 between cases with higher wall heat fluxes and those with lower heat fluxes. With increasing heat flux, ONB commences farther upstream near to the inlet due to increasing wall superheat. Earlier nucleation at higher heat fluxes also precipitates faster bubble growth along with more aggressive bubble detachment, culminating in earlier transition of flow regime from bubbly to churn-slug. Note for the largest heat flux case that the regime transition happens within the upstream region, which leads to formation of wavy vapor layers downstream along the heated wall. These wavy vapor layers feature middle peak – crest – surrounded by troughs – wetting fronts - where sufficient core liquid is able to replenish the heated wall and maintain stable wall temperatures. Presumably, further increases in wall heat flux will "extinguish" the liquid replenishment by merging adjacent vapor waves, leading to formation of a continuous thermally insulating vapor layer covering most of the heated length, an ob-

vious precursor for CHF. This depiction of interfacial behavior is supportive of premises of the *Interfacial Lift-off CHF Model* [68].

4.2.2. Fluid temperature predictions

Fig. 12 shows computed fluid temperature along the heated length of the test section for the four sets of operating conditions. These contour plots show an instantaneous temperature field after achieving numerical steady state. As described earlier, all four cases have nearly identical mass velocities, slightly subcooled inlet conditions, and the same saturation temperature of $T_{sat} = 89.5$ K (based on the single inlet pressure measurement provided in benchmark experiments). As expected, Fig. 12 shows the subcooled liquid core penetrates farther downstream with decreasing heat flux because of delayed thermal boundary layer development. In the ensuing bubbly flow region, bubble nucleation and detachment become primary sources for thermal energy transfer from heated wall to subcooled liquid core. With increasing heat flux, superheated vapor bubbles detaching from the heated wall and migrating into the core cause earlier increase in subcooled liquid temperature as well as earlier attainment of saturation temperature. Notice for the highest heat flux case how the superheated thermal boundary layer starts right after the inlet and the liquid core temperature rapidly increases with more aggressive heat transfer from the superheated vapor bubbles.

4.3. Validation of computed results

4.3.1. Wall temperature comparison

To validate accuracy of the present CFD method, predicted wall temperatures from simulations are compared to measured wall temperatures from Lewis et al. [13]. Fig. 13 shows wall temperature variations along the heated portion of the experiment facility along with the numerical predictions for the four different test cases. Predicted wall temperature results are time averaged for several seconds after achieving steady state convergence. Note again that the four mass fluxes considered are within a $\pm 2\%$ range, leaving only wall heat flux as variable.

For all four cases, the predicted curves show similar behavior: nearly constant wall temperature with slight perturbation. The constant wall temperature trend is rooted in the fact that all four cases feature near-saturated inlet temperature, which allows two-phase heat transfer to play a dominant role starting from the upstream region. Note that perturbation of wall temperature is increasing with increasing heat flux presumably because of vapor pockets near the heated wall causing localized interruption to liquid replenishment and therefore local increases in wall temperature.

Fig. 13 shows minimal differences between predicted and measured average wall temperatures, 0.39, 0.08, 0.19, and 1.67 K, increasing monotonically with increasing heat flux. The highest difference corresponding to the highest wall flux case implies the simulations slightly overestimate the effect of vapor layer accumulation and therefore predict higher wall temperatures than measured.

It must be noted here that previous CFD simulations [40–42] of flow boiling employing VOF have yielded significantly higher wall temperature deviations. A key reason for this departure is inaccurate surface tension calculations culminating in excessive accumulation of vapor pockets near the heated wall. This shortcoming is overcome in the present CLSVOF simulations with better interface tracking and more accurate surface tension calculations, thereby rectifying the commonly encountered weakness of VOF in the form of artificial vapor adhesion to the heated wall as explained in Section 1.2.2. Additionally, with inclusion of BCD force in the CLSVOF model, under-represented bubble-to-bubble interac-
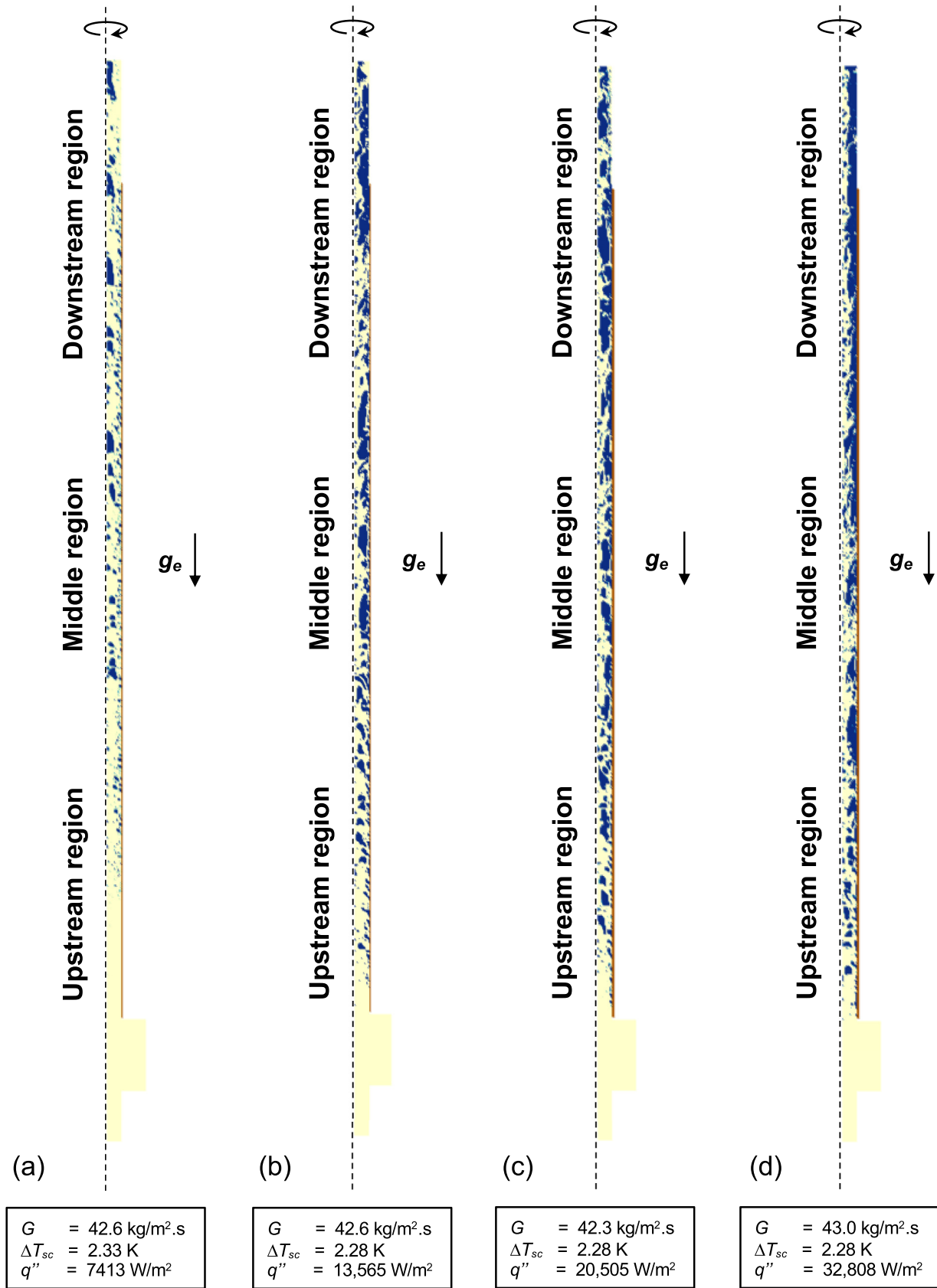
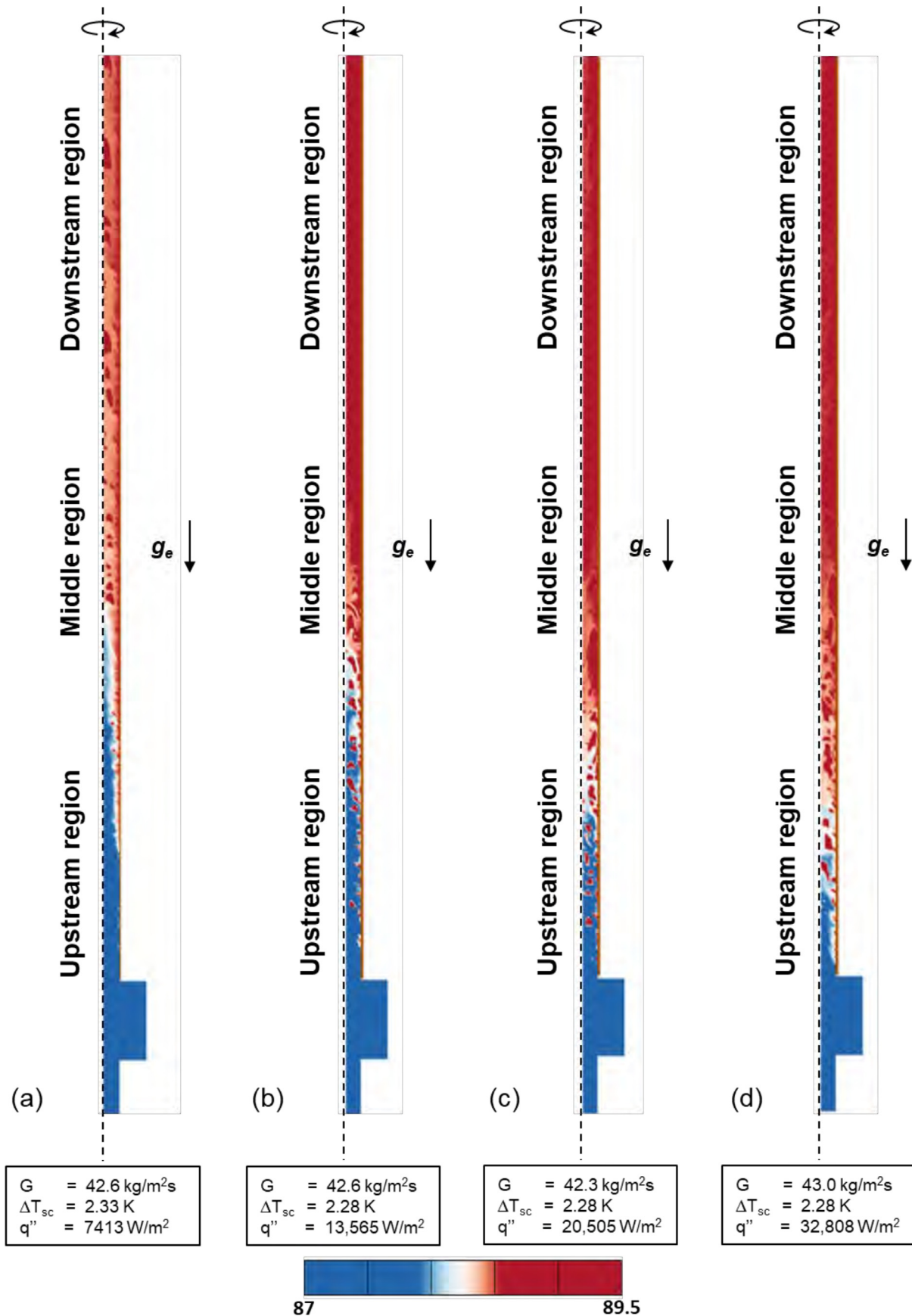**Fig. 11.** Computationally predicted flow visualization images of entire heated channel for different heat fluxes.

(a)	(b)	(c)	(d)
G = 42.6 kg/m²s	G = 42.6 kg/m²s	G = 42.3 kg/m²s	G = 43.0 kg/m²s
ΔT_{sc} = 2.33 K	ΔT_{sc} = 2.28 K	ΔT_{sc} = 2.28 K	ΔT_{sc} = 2.28 K
q" = 7413 W/m²	q" = 13,565 W/m²	q" = 20,505 W/m²	q" = 32,808 W/m²

Fig. 12. Computationally predicted fluid temperature field of entire heated channel for different heat fluxes.
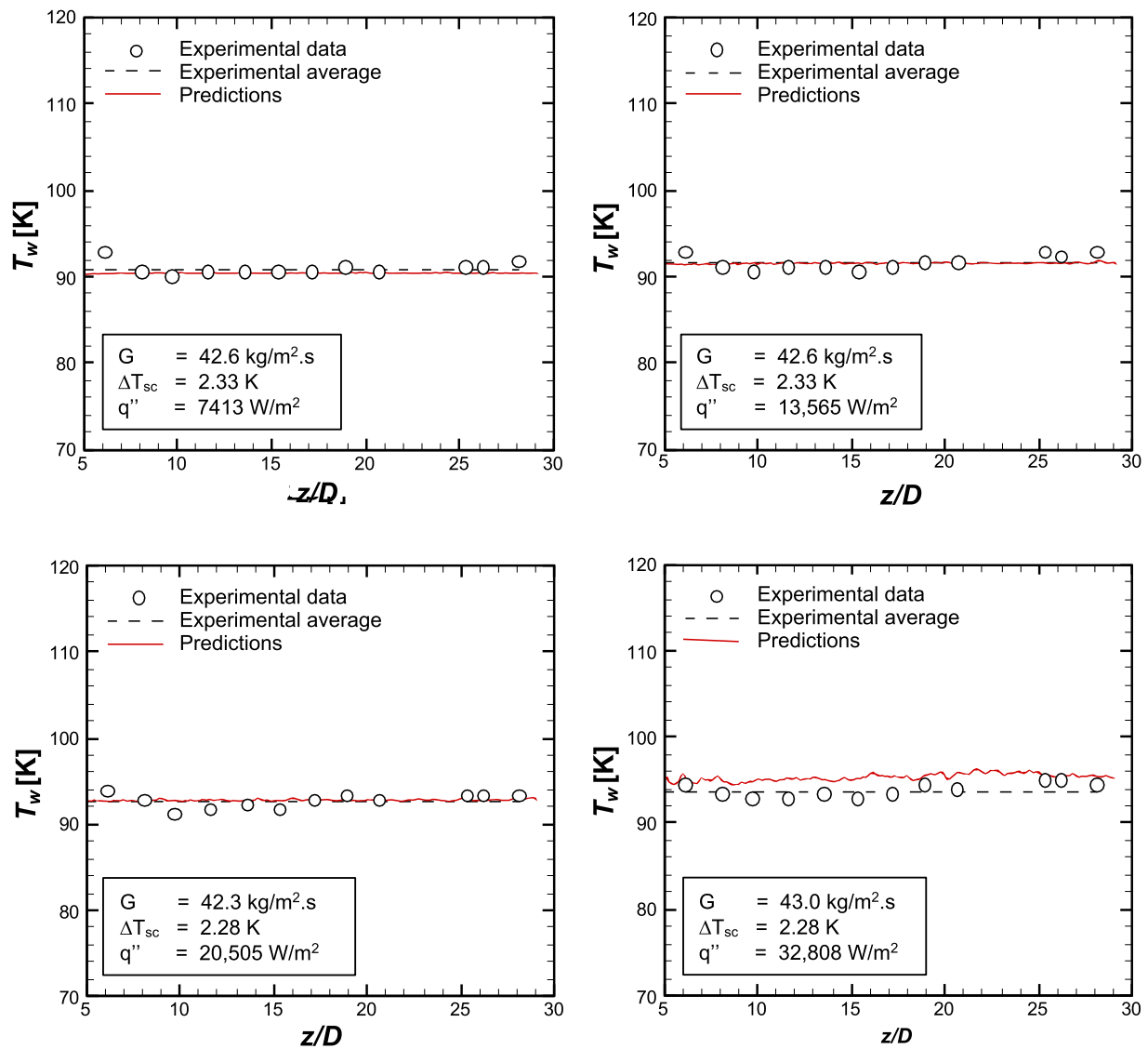
Fig. 13. Comparison of measured axial variation of wall temperature with predictions from present simulations.

tions such as dispersion due to bubble collision are counterpoised, further enhancing accuracy of the wall temperature predictions.

4.3.2. Area-averaged volume of fraction comparison

It is a well-known fact in cryogenic flow boiling studies that it is extremely difficult to acquire flow visualization records. Due to this fact, most previous researchers had to rely on measurable data to understand fluid flow physics. The benchmark experiments also did not provide flow visualization results with which to compare flow contours from the present numerical simulations. Instead, the benchmark experiments provided values of thermodynamic equilibrium quality, x_e, at the outlet of the test section. Using this quality information, the present authors obtained void fraction information at the outlet of the test section using the popular Zivi correlation [69],

$$\alpha = \left[1 + \left(\frac{1 - x_e}{x_e} \right) \left(\frac{\rho_g}{\rho_g} \right)^{2/3} \right]^{-1} \tag{14}$$

Fig. 14 compares the void fraction at the end of the heated length with spatially and time-averaged predicted void fraction along the heated test section for the four sets of operating conditions. The predicted axial variations are especially useful for deter-

mining dominant local two-phase flow regime. For the lowest wall heat flux of $q'' = 7413$ W/m^2, predicted void fraction monotonically increases in the axial direction, with experimental exit value well predicted by the simulations. A similar trend is captured for $q'' = 13565$ and 20505 W/m^2, but with higher void fractions predicted farther upstream, but with only moderate change beginning at $z \sim 0.2$ m. For the highest flux of $q'' = 32808$ W/m^2, exit values approach unity, indicating even further development of flow regime from those for the two intermediate heat fluxes.

The predicted void fraction results correspond well with the flow contours described in Section 4.2.1 in conjunction with Fig. 11. For the lowest wall heat flux of $q'' = 7413$ W/m^2, void fraction at $z = 0.1$ m is quite small, indicative of ONB occurring in the inlet region as depicted in the corresponding flow contour in Fig. 11. Additionally, the steep increase of void fraction matches well with the transition of flow regime from dispersed bubbly to churn-slug along the axial direction. For $q'' = 13565$ and 20505 W/m^2, both Figs. 11 and 14 show ONB occurs much closer to the inlet, allowing large bubbles to form farther upstream. Also, for both cases, a transition from small, dispersed bubbles to larger oblong bubbles takes effect in the region of $z = 0.2$ to 0.4 m, which is reflected both in the contour plots, Fig. 11, and magnitude of void fraction,
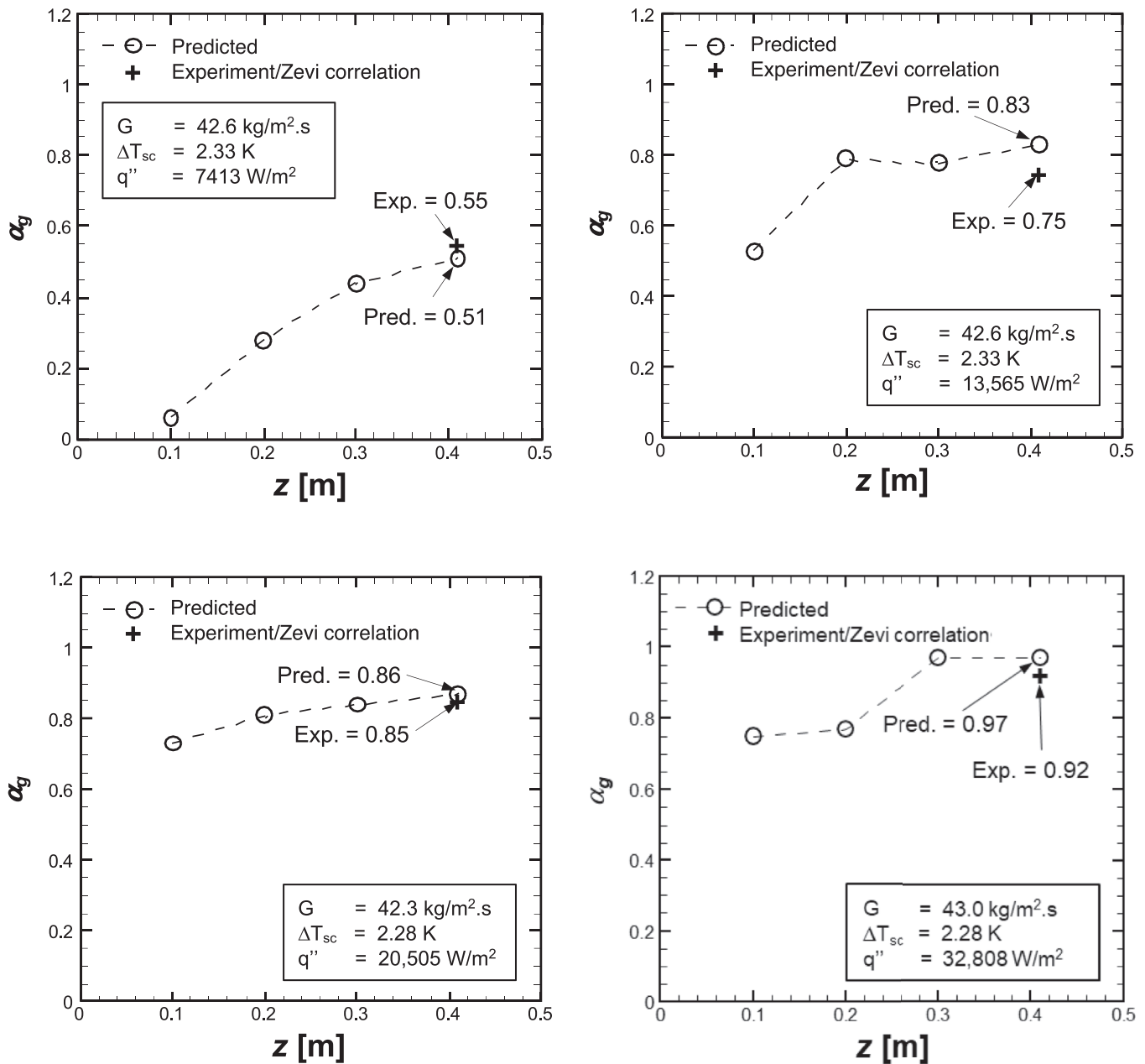
Fig. 14. Comparison of area-averaged void fraction predictions with those of experiment and Zivi correlation.

Fig. 14. Lastly, for the highest flux of $q'' = 32808$ W/m^2, after more rapid development of the large oblong bubbles farther upstream, there is yet further flow regime development of much larger void fraction downstream, along with formation of wavy vapor layers along the heated wall as captured in Fig. 11. These observations are supported in Fig. 14 by a steep increase in volume fraction in the middle region, followed by values approaching unity for the downstream region containing the massive vapor formations in the core along with wavy vapor layers along the heated wall.

Predicted volume fractions for the given operating conditions were compared to the calculated volume fraction based on experimental data. Based on the comparison results shown in Fig. 14, the present numerical simulation well predicts volume fraction at the end of the heated section showing the minimal differences to the experimental data. The minimum difference was shown with mass velocity of 42.3 kg/m^{2}s, inlet subcooling of 2.28K and with wall heat flux of 20505 W/m^2 which corresponds to 40% of CHF.

Fig. 15 compares predicted void fraction profiles both with and without BCD force for $G = 42.6$ kg/m^{2}s, $q'' = 13,565$ W/m^2, and $\Delta T_{sc} = 2.28$ K. Without BCD force, because of excessive bubble coalescence, void fraction monotonically increases resulting in a void fraction approaching unity, which deviates appreciably from experiment. Whereas with BCD force, outlet void fraction is appreciably smaller and shows smaller deviation from experiment. This is proof that inclusion of BCD force in two-phase simulations provides better representation of flow pattern evolution along the heated tube than the case without BCD force.

4.4. Predicted velocity and temperature profiles

4.4.1. Temperature profile

Fig. 16 shows instantaneous radial profiles of computed fluid temperature at four different axial locations ($z = 0.1, 0.2, 0.3, 0.4$ m) for the four sets of operating conditions. These profiles are
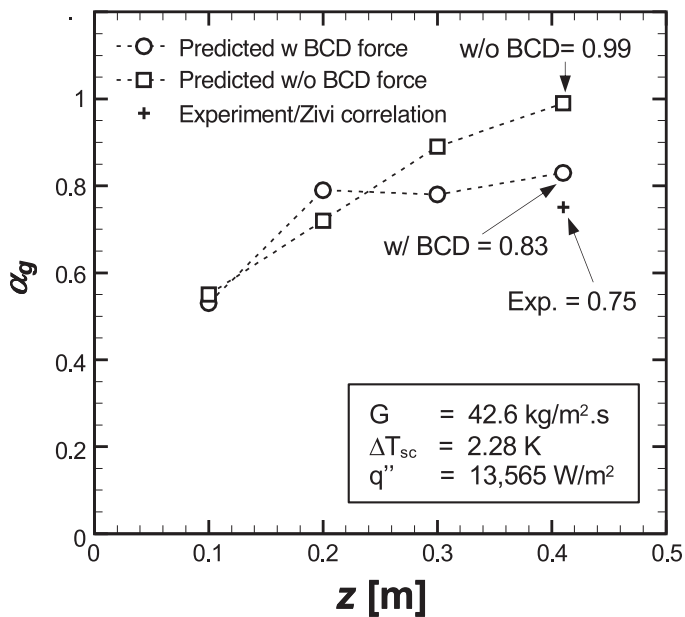
Fig. 15. Comparison of axial volume fraction profiles for simulations with and without inclusion of BCD force. Operating conditions are $G = 42.6$ kg/m^2.s, $q'' = 13565$ W/m^2, and inlet subcooling of $\Delta T_{sc} = 2.28$ K.

extracted after steady state. Readily observable for all four test cases is how the upstream region from inlet to $z = 0.2$ m contains an appreciable temperature gradient between the wall region and slightly subcooled liquid core. Starting at $z = 0.2$ mm, radial temperature gradients subside appreciably as fluid temperature is maintained near the saturation temperature of 89.5 K for the given pressure.

For the lowest wall heat flux of $q'' = 7413$ W/m^2, the radial temperature profile at $z = 0.1$ m is indicative of a developing thermal boundary layer with steep gradient near the heated wall. Within the thermal boundary layer adjacent to the wall, tiny bubbles are nucleating but are not sizable enough to detach. It is just outside of the radial region occupied by these bubbles that the temperature rises appreciably compared to the liquid core before stabilizing to a rather flat radial profile with sharp gradient confined only to close vicinity of the wall. Except the sharp gradient in the small wall region, fluid temperature rapidly increases along the axial direction, approaching saturation. This is a direct outcome of better ability of bubbles to detach into and produce appreciable mixing in the core for $z = 0.2 - 0.4$ m. For $q'' = 13565$ W/m^2, at $z = 0.1$ m, the radial temperature profile is marred by a radial span where fluid temperature increases appreciably compared to the subcooled liquid core. This can be explained by nucleating bubbles now growing more appreciably in size and are therefore able to detach and mix with core liquid farther away from the wall than for $q'' = 7413$ W/m^2. There is also a reduction in fluid temperature farther toward the wall where liquid trapped between the bubble layer and wall resumes its initial thermal boundary layer development from the inlet. And, like $q'' = 7413$ W/m^2, excepting the sharp gradient in close proximity to the wall, fluid temperature rapidly increases for $z = 0.2 - 0.4$ m, approaching saturation. Similar trends are observed at $z = 0.1$ m for $q'' = 20505$ W/m^2, with one obvious deviation. Here, the large intermediate radial temperature increase has expanded farther toward both the central axis and heated wall, indication of detached bubbles growing larger in size, penetrating deeper into the liquid core, and occupying a larger fraction of the flow area; this also points to flow regime transition from dispersed bubbly to oblong bubbles/churn-slug as

depicted in Fig. 11. For the same heat flux, trends for $z = 0.2 - 0.4$ m are similar to those for the lowest two heat flux cases. For the highest wall heat flux of $q'' = 32808$ W/m^2, radial profile at $z = 0.1$ m features substantial deviations from those for the three lower heat flux cases, caused by formation of wavy vapor layers now covering portions of the heated wall. The vapor layers compromise ability of core liquid to replenish the wall, thereby decreasing heat transfer effectiveness, which is evidenced by the fluid temperature rising well above saturation for $z = 0.3$ and 0.4 m.

4.4.2. Velocity profile

To accurately capture test section inlet conditions for the benchmark experiments, geometrical characteristics of the inlet must be carefully understood and simulated. As shown in Fig. 6, the experimental heated section is preceded by an inlet chamber which provides sudden expansion and contraction before entering the heated section. This abrupt change of cross-sectional area causes drastic velocity profile changes from the fully developed velocity profile. Failure to account for these changes will undoubtedly compromise not only flow physics at the inlet to the heated section but heat transfer as well. This explains inclusion of the fluid domain of the inlet chamber in the present simulations. Note that, as explained in Section 2.4, to initiate the numerical simulations, a fully developed velocity profile is designated for the velocity boundary condition at the entrance to the inlet chamber, not the heated section.

Fig. 17 shows radial profiles of computed fluid velocity at four axial locations for the four test conditions. These profiles are extracted after attaining steady state along the radial axis for all the axial locations. Note that the mass velocity conditions correspond to a very narrow Reynolds numbers range between 3426 and 3556, indicating flow near the heated section inlet is in transition from laminar to turbulent flow. Overall, all four wall heat flux cases in Fig. 16 show velocity generally increasing along the axial direction, an outcome of acceleration caused by the axial increase in vapor fraction resulting from the bubble formation. However, there are noticeable instantaneous profile variations among axial locations. For $q'' = 7413$ W/m^2, with limited bubble detachment, the profile variations are comparatively weak. As bubbles grow larger and detach into the core for $q'' = 13565$ W/m^2, the now faster moving bubbles increase velocity over the region from $r = 3$ mm to the wall. Similar trends are captured for $q'' = 20505$ W/m^2, albeit with greater overall axial acceleration. For the highest heat flux of $q'' = 32808$ W/m^2, effects of faster moving oblong bubbles are felt even closer to the axis and with greater fluctuation intensity. Also noticeable, especially for the highest two heat fluxes, is a rather large increase in velocity closer the wall, outcome of formation of wavy vapor layers in the same radial region.

4.5. Boiling curve

Based on computed steady state wall temperature results, a partial boiling curve is generated for the four wall heat flux conditions, which range from 14% to 63% of experimentally measured CHF. Shown in Fig. 18, the boiling curve is plotted as wall heat flux versus wall superheat, the latter defined as wall temperature, T_w, minus saturation temperature, T_{sat}. Predicted boiling curves are generated for five different axial locations, $z = 0.05, 0.1, 0.2, 0.3$, and 0.4 m. Note that predictions for $z = 0.05$ m are included to show transition from single-phase forced convective to nucleate boiling. By analyzing these boiling curve segments, it is possible to infer information concerning both the actual experiments and simulation results. First, the slope of the curve in this logarithmic plot is almost constant throughout the range of wall heat flux, which indicates a dependence of the form $q'' \sim (T_w - T_{sat})^n$. This
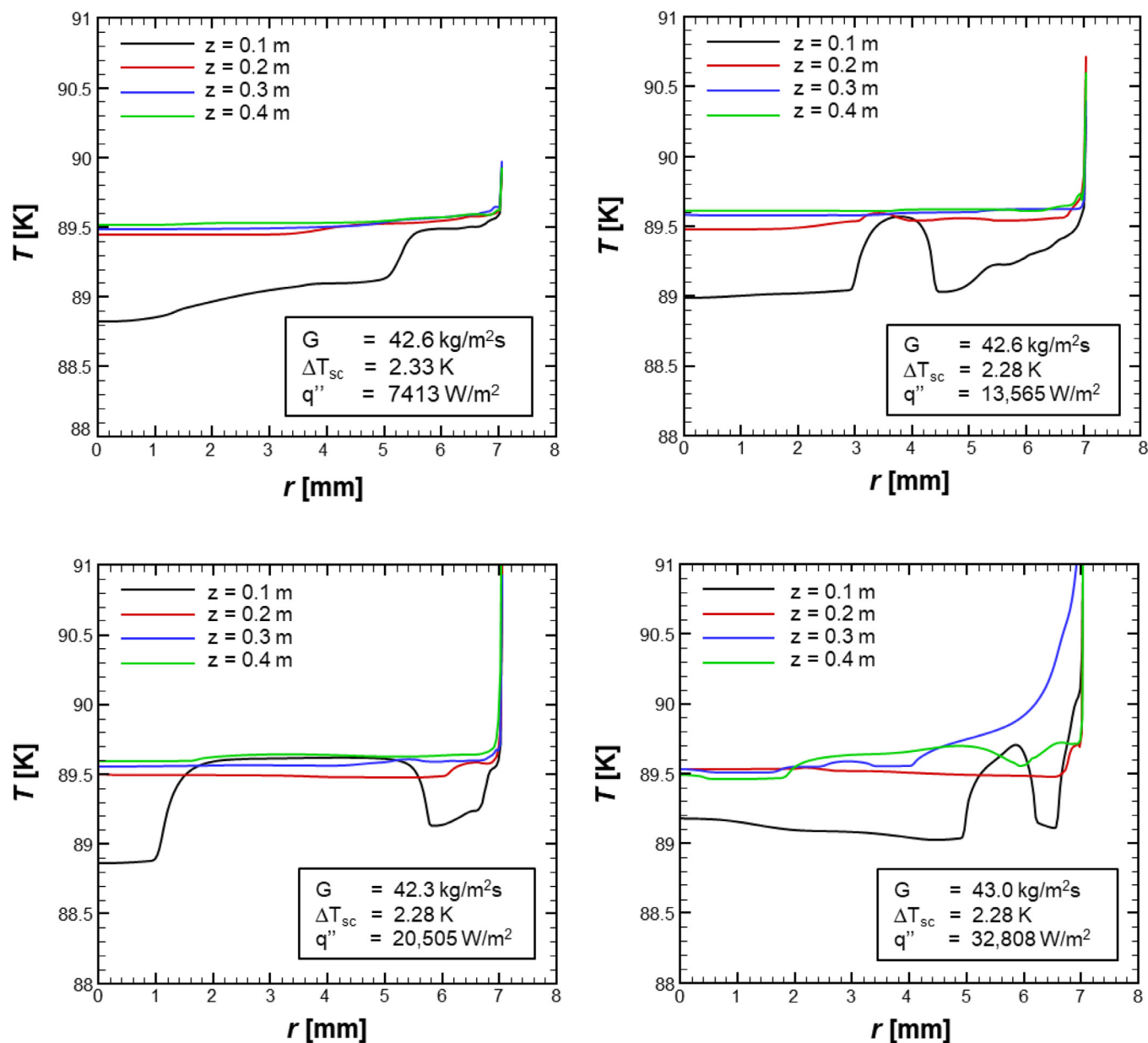
Fig. 16. Instantaneous computed fluid temperature profiles across the axisymmetric channel for four axial locations for the different operating test conditions.

suggests heat transfer is maintained well within the nucleate boiling regime along the heated test section, which is confirmed by interfacial behavior and flow regimes described in earlier sections. Second, by comparing the curve for $z = 0.05$ m to the rest of the boiling curves, it is notable that the slope of the boiling curve increases as wall heat flux is increased from 14% to 26% CHF but becomes nearly constant above 26% CHF. For 14% CHF, due to low wall heat flux, very few bubbles are nucleating on the heated wall at $z = 0.05$ m, which is close to the ONB point and therefore corresponds to partial nucleate boiling, where both sensible heat and latent heat contribute appreciably to heat transfer. For the same location of $z = 0.05$ m, convergence with results for the downstream locations starting at 26% CHF indicates transition to fully developed nucleate boiling; this is where heat transfer is dominated by latent heat. Another observation from Fig. 16 is a slight diminution of slope for the 63% CHF case. As explained earlier, with development of wavy vapor layers on the heated wall, heat transfer is compromised, which increases wall temperature. The captured de-

gressive trend is often cited as Onset of Nucleate Boiling Degradation (ONBD), a precursor to CHF, which occurs upon further increases in wall heat flux.

5. Limitations of two-phase simulations

In real-life applications, cavities are known to randomly span a heated wall, and bubble nucleation occurs in cavities having relatively large initial vapor embryos after acquiring sufficient liquid superheat at the wall. As shown in Table 6, most of the previous two-phase simulation efforts employed a combination of VOF and Lee model without accounting for actual cavity nucleation effects. There are several challenges to incorporating effects of the surface cavities. First, unlike recent works, effects of cavity activation are incorporated using artificial empirical functions rather than measured cavity distributions. Second, even when attempting to incorporate the effects of actual cavities, available physical models for cavity activation are based on exitance of a relatively large vapor

Table 6

Previous numerical studies for two-phase flow boiling simulations with and without artificial nucleation site modeling.

| Authors	Year	Fluid	Application	Multiphase model	Phase change model	Artificial nucleation site or bubble(s)	Remark
Yeo et al. [63]	2022	FC-72	Microchannel heat sink	VOF	Lee model ($r_i = 500$ [1/s])	No	- Tuned relaxation parameter (r_i) to address heterogeneous nucleation
Lin et al. [73]	2021	water	Micro-fin / micro-cavity microchannel flow boiling	VOF	Lee model ($r_{i.evap} = 10^2$ [1/s]) ($r_{i.cond} = 10^6$ [1/s])	No	- Wettability comparison with or without micro-structured surface - Tuned relaxation parameter (r_i) to address heterogeneous nucleation
Broughton and Joshi [74]	2021	water	Microchannel flow boiling	VOF	Lee model ($r_i = 75$ [1/s])	No	- Single sided heating with horizontal orientation - 3D Conjugated heat transfer problem - Tuned relaxation parameter (r_i) to address heterogeneous nucleation
Dong et al. [75]	2019	water	Subcooled flow boiling	VOF	Novel phase change model (λ=0.1 [1/s])	No	- Developed novel phase change model based on Lee model - Requires empirical accommodation factor, λ
Lorenzini and Joshi [76]	2019	HFE-7200	Microgap flow boiling	CLSVOF	Lee model ($r_i = 100$ [1/s])	No	- Single sided heating with horizontal orientation - 3D Conjugated heat transfer problem - Tuned relaxation parameter (r_i) to address heterogeneous nucleation
Lorenzini and Joshi [77]	2018	water	Microchannel flow boiling with non-uniform heat flux	VOF	Lee model ($r_i = 0.1$ [1/s])	No	- Single sided heating with horizontal orientation - 3D Conjugated heat transfer problem - Tuned relaxation parameter (r_i) to address heterogeneous nucleation
Mohammed et al. [78]	2018	Acetone with nanoparticles	Nanofluid flow boiling	VOF	Lee model (N/A)	No	- Single sided heating with horizontal orientation - Tuned relaxation parameter (r_i) to address heterogeneous nucleation
Prajapati et al. [79]	2017	water	Finned microchannel flow boiling	VOF	Lee model (N/A)	No	- Tuned relaxation parameter (r_i) to address heterogeneous nucleation
Bahreini et al. [80]	2017	HFE-7100	Subcooled flow boiling	VOF	Lee model ($r_i = 1$ [1/s])	No	- Microgravity flow boiling - 2D Conjugated heat transfer problem - Truncation error in numerical simulation creates random distribution of vapor nucleation sites - Tuned relaxation parameter (r_i) to address heterogeneous nucleation
Cheung et al. [81]	2014	water	Subcooled flow boiling	Two-fluid model	Heat flux partitioning model	No	- Assessed various combinations of empirical closure correlations - Revealed existing correlations for nucleation site density, bubble departure frequency, and bubble departure diameter cannot provide satisfactory predictions
Chen et al. [82]	2022	water	Microchannel flow boiling	VOSET	Interface heat conduction	Yes (Artificial nucleation sites)	- Empirical correlations for nucleation site density for water - Artificial and random designation of cavity location - Artificial bubble patching on activate cavity
Vontas et al [83]	2021	Ethanol	Single bubble growth in microchannel	VOF	Novel phase change model	Yes (Single bubble / multiple bubbles)	- Patched a single half-sphere bubble on heated wall - Patched 29 half-sphere bubbles on heated wall
Bahreini et al. [84]	2015	water	Single bubble analysis	VOF	Lee model ($r_i = 100$ [1/s])	Yes (Single bubble)	- Patched single bubble in subcooled flow - Bubble condensation
Zu et al. [85]	2011	water	Confined bubble growth in microchannel	VOF	N/A	Yes (Bubble injection)	- Pseudo-nucleate boiling - Bubble injection to mimic bubble nucleation and departure - Arbitrary injection time
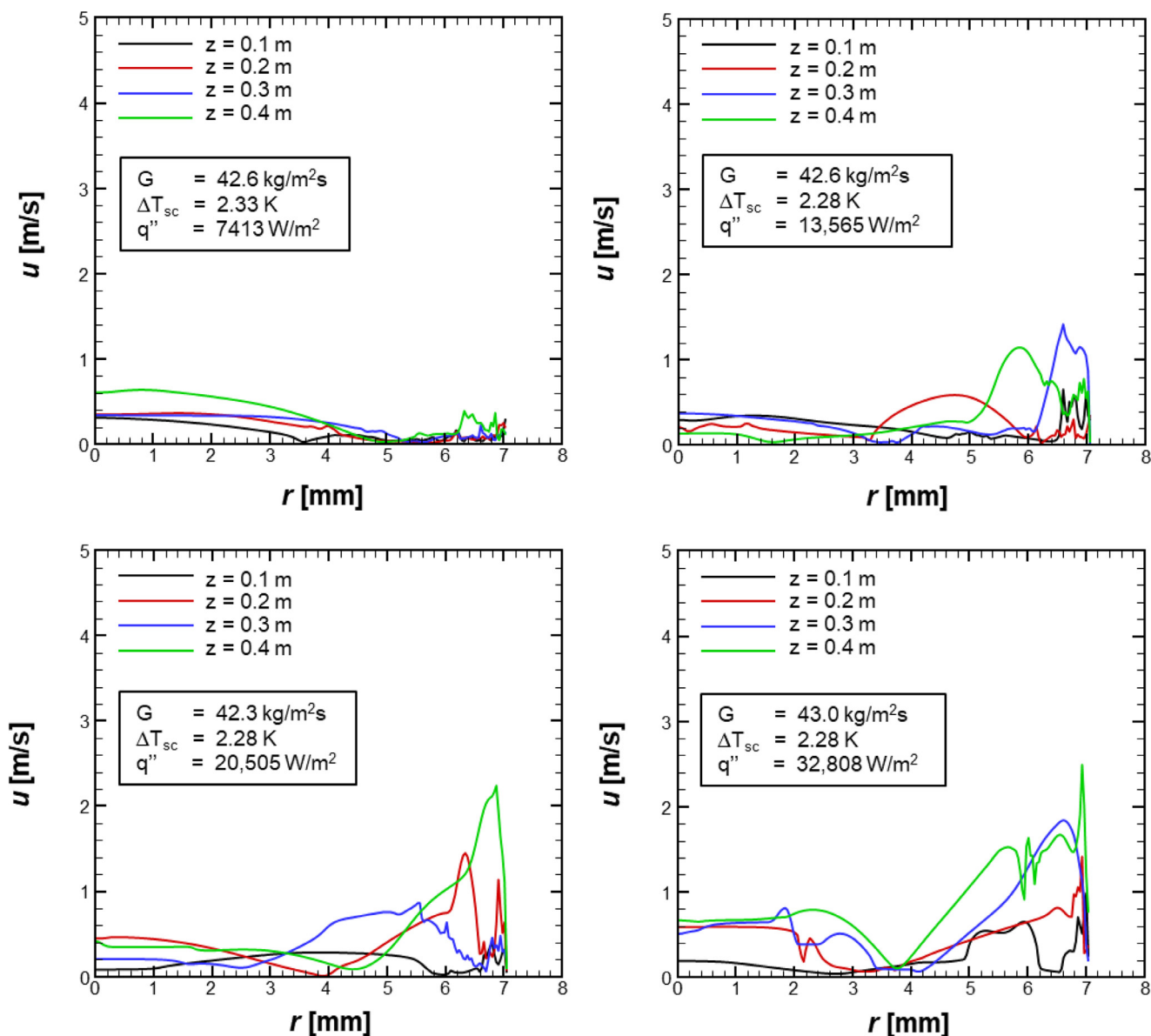
Fig. 17. Instantaneous computed fluid velocity across the axisymmetric channel for four axial locations for the different operating test conditions.

embryo within the cavity. While this is valid for common fluids such as water, the same models are inapplicable to fluids having small contact angles such liquid nitrogen (fluid modeled in the present study) which have tendency to penetrate deep into cavities, precluding formation of a large initial vapor embryo. Thirdly, large-scale flow boiling simulations such as those presented in the present study are computationally both time consuming and expensive. Attempts to include effects of actual surface cavities are expectedly computationally prohibitive, requiring many months to yield a solution for even a single set of operating conditions. Recall that a key objective of modern flow boiling simulations is to devise models that are very robust when modeling actual devices and systems.

As shown in Table 6, the Lee model is deemed by most as plausible approach to numerically address heterogeneous nucleation effects when computing rate of vaporization by tuning the so-called relaxation parameter r_i. A key advantage of this model is reliance on the assumption that interfacial mass transfer is driven by difference between local temperature and saturation temperature, which provides simplicity and highly reduced computation

time and cost especially for large-scale simulations, without having to account for actual surface cavities. In this paper, the same r_i value is adopted for the entire flow field without distinguishing the bulk liquid region and near wall region. There are several advantages to using this methodology. First, with varying r_i value by location, numerical stability degrades dramatically due to an abrupt change of mass transfer rate between cells inducing numerical divergence. Second, since inlet subcooling is very small, less than 3K, non-equilibrium effects across the flow area are miniscule. This is captured in Fig. 11 which shows a rapid increase of bulk fluid temperature to saturation. Third, in the Lee model, according to Eq. (6), mass transfer is dictated not only r_i value but liquid superheat as well. As the liquid superheat increases close to the heated wall, the amount of mass transfer will increase more for the wall region than the channel core.

Table 6 summarizes previous numerical studies on two-phase flow and heat transfer. As indicated above, majority of these rely on combination of VOF and Lee model to predict both interfacial mass transfer and account for heated wall nucleation. According to Bahreini et al. [80], truncation error in the numerical simula-
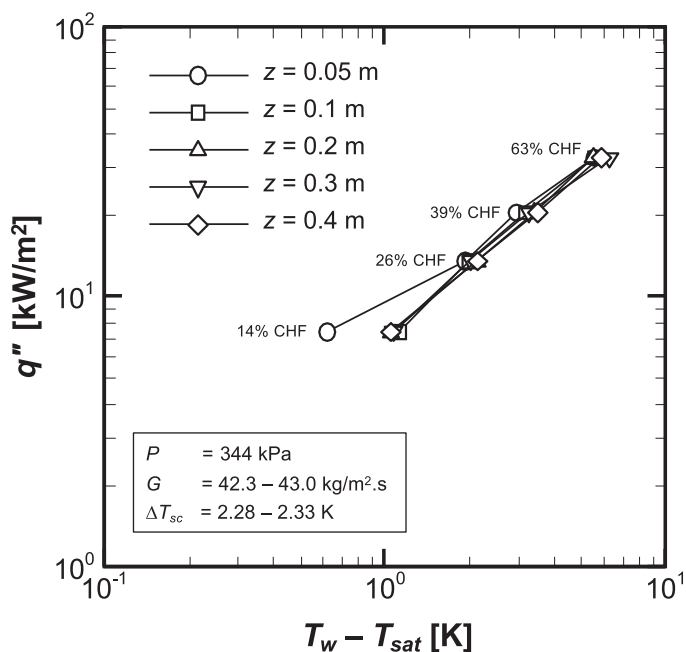
Fig. 18. Predicted segments of boiling curve for different heat fluxes and $z = 0.05$ – 0.4 m for indicated operating conditions.

tion creates a random distribution of vapor bubble nucleation sites along the heated wall enables the Lee model to adequately address phase change along the heated wall. Chen et al. [82] created artificial nucleation sites along the heated wall based on empirical correlations which were experimentally developed using water as working fluid. Artificial cavities were randomly distributed, and nucleation criteria imposed on each category of cavities. Furthermore, studies utilizing artificial cavities or artificially patched bubbles on heated surfaces involve mostly small domain two-phase configurations such as the single bubble growth studies by Bahreini et al. [84] and Zu et al. [81], rather than large-scale simulations.

However, since such correlations are entirely water specific, they simply cannot be adopted in cryogenic flow boiling simulations. Incorporating the same effects in cryogenic fluid simulations would require careful measurements of bubble departure diameter, bubble nucleation site density, and bubble departure frequency for each combination of cryogenic fluid and solid wall material combination.

6. Conclusions

The present study focused on implementation of a 2-D axisymmetric CFD method to investigate near-saturated upflow boiling of liquid nitrogen along a vertical heated tube. This method employs the Coupled Level Set VOF (CLSVOF) model, which is adopted in ANSYS FLUENT, including a user defined function to account for crucial effects of bubble collision dispersion (BCD) force. The simulation predictions were validated against four sets of operating conditions from prior benchmark experiments with heat fluxes of 7413, 13565, 20505, and 32808 W/m², and very narrow range of mass velocity of 42.3 – 43.0 kg/m².s. The simulations proved effective at capturing important flow and heat transfer characteristics, including axial variations of interfacial behavior and local flow regime, as well as both fluid temperature and fluid velocity, information that is very difficult to obtain from cryogen boiling experiments. Key findings from study are as follows:

(1) The CFD simulations captured crucial details of flow boiling behavior along the heated tube, including bubble nucleation, slid-

ing, growth, departure, dispersion, and coalescence. Predicted wall temperatures for the four sets of operating conditions showed excellent agreement with the benchmark experimental data. Additionally, very good agreement was achieved between exit volume fraction predictions and experiment.

(2) Bubble collision dispersion force was shown highly effective at overcoming innate limitations of single momentum equation models known to under-represent relative motion between phases. Inclusion of the BCD force was shown to limit coalescence of small bubbles following bubble-to-bubble collision as well prevent premature prediction of CHF resulting from excessive vapor blanketing downstream. It was shown that BCD effects are prevalent mostly in the region of small dispersed bubbles but are far less significant for large bubbles where interface area per vapor volume decreases appreciably thereby reducing BCD force.

(3) Presented were predictions for axial evolution of both fluid velocity and fluid temperature profiles. The temperature profiles capture formation of a superheated thermal boundary layer in the inlet region which gradually penetrates the channel core until core temperature reaches saturation. Viewed in conjunction with the fluid velocity profiles, the temperature profiles also capture effects of bubble dynamics both across and along the heated pipe.

(4) The present computational methodology shows excellent predictive accuracy when compared to liquid nitrogen data and may therefore constitute a good foundation for predicting flow boiling characteristics for other cryogens for which experimental data range from sparse to nonexistent.

Declaration of Competing Interest

None. The authors declare that they have no known competing financial interests or personal relationships that could have appeared to influence the work reported in this paper.

Data availability

The data that has been used is confidential.

References

[1] T.J. Laclair, I. Mudawar, Thermal transients in a capillary evaporator prior to the initiation of boiling, Int. J. Heat Mass Transf. 43 (2000) 3937–3952.

[2] I. Mudawar, T.M. Anderson, Parametric investigation into the effects of pressure, subcooling, surface augmentation and choice of coolant on pool boiling in the design of cooling systems for high-power-density electronic chips, J. Electron. Packag. 112 (1990) 375–382.

[3] I. Mudawar, R.A. Houpt, Mass and momentum transport in smooth falling liquid films laminarized at relatively high Reynolds numbers, Int. J. Heat Mass Transf. 36 (1993) 3437–3448.

[4] C.O. Gersey, I. Mudawar, Effects of heater length and orientation on the trigger mechanism for near-saturated flow boiling critical heat flux - II. Critical heat flux model, Int. J. Heat Mass Transf. 38 (1995) 643–654.

[5] S. Mukherjee, I. Mudawar, Pumpless loop for narrow channel and micro-channel boiling, J. Electron. Packag. 125 (2003) 431–441.

[6] J. Lee, I. Mudawar, Fluid flow and heat transfer characteristics of low temperature two-phase micro-channel heat sinks – Part 2: subcooled boiling pressure drop and heat transfer, Int. J. Heat Mass Transf. 51 (2008) 4327–4341.

[7] M.E. Johns, I. Mudawar, An ultra-high power two-phase jet-impingement avionic clamshell module, J. Electron. Packag. 118 (1996) 264–270.

[8] W.P. Klinzing, J.C. Rozzi, I. Mudawar, Film and transition boiling correlations for quenching of hot surfaces with water sprays, J. Heat Treat. 9 (1992) 91–103.

[9] M.K. Sung, I. Mudawar, Single-phase and two-phase heat transfer characteristics of low temperature hybrid micro-channel/micro-jet impingement cooling module, Int. J. Heat Mass Transf. 51 (2008) 3882–3895.

[10] J. Hartwig, S. Darr, A. Asencio, Assessment of existing two phase heat transfer coefficient and critical heat flux correlations for cryogenic flow boiling in pipe quenching experiments, Int. J. Heat Mass Transf. 93 (2016) 441–463.

[11] V. Ganesan, R. Patel, J. Hartwig, I. Mudawar, Review of databases and correlations for saturated flow boiling heat transfer coefficient for cryogens in uniformly heated tubes, and development of new consolidated database and universal correlations, Int. J. Heat Mass Transf. 179 (2021) 121656.

[12] V. Ganesan, R. Patel, J. Hartwig, I. Mudawar, Universal critical heat flux (CHF) correlations for cryogenic flow boiling in uniformly heated tubes, Int. J. Heat Mass Transf. 166 (2021) 120678.

[13] J.P. Lewis, J.H. Goodykoontz, J.F. Kline, Boiling heat transfer to liquid hydrogen and nitrogen in forced flow, NASA Technical Note D-1314 (1962).

[14] S.S. Papell, Buoyancy effects on liquid nitrogen film boiling in vertical flow, NASA TECHNICAL PAPER G-2 (1970).

[15] D. Steiner, E.U. Schlunder, Heat transfer and pressure drop for boiling nitrogen flowing in a horizontal tube 1. Saturated flow boiling, Cryogenics 16 (1976) 387–398.

[16] D. Steiner, E.U. Schlunder, Heat transfer and pressure drop for boiling nitrogen flowing in a horizontal tube 2. Pressure drop, Cryogenics 16 (1976) 457–464.

[17] H.M. Muller, W. Bonn, D. Steiner, Heat transfer and critical heat flux at flow boiling of nitrogen and argon within a horizontal Tube, in: Proceedings of the Advanced Course in Heat Exchangers: Theory and Practice. ICHMT Symposium, 1981, pp. 233–250.

[18] W. Bonn, R. Krebs, D. Steiner, Kritishe Warmestromdichte bei der Zweiphasenstromung von Skickstoff imwaagerechten Rohr bei Drucken bis zum kritischen Druck, Warme Stoffubertrag. 13 (1980) 265–274.

[19] S.S. Papell, R.C. Hendricks, Boiling incipience and convective boiling of neon and nitrogen, NASA Technical Memorandum (1977).

[20] V.V. Klimenko, Heat transfer intensity at forced flow boiling of cryogenic liquids in tubes, Cryogenics 22 (1982) 569–576.

[21] V.V. Klimenko, A.M. Sudarchikov, Investigation of forced flow boiling of nitrogen in a long vertical tube, Cryogenics 23 (1983) 379–385.

[22] J.C. Chen, Correlation for boiling heat transfer to saturated fluids in convective flow, Ind. Eng. Chem. Process Des. Dev. 5 (1966) 322–329.

[23] M.M. Shah, A new correlation for heat transfer during boiling flow through pipes, ASHRAE Trans. 82 (1976) 66–86.

[24] M.M. Shah, Prediction of heat transfer during boiling of cryogenic fluids flowing in tubes, Cryogenics 24 (1984) 231–236.

[25] W.M. Rohsenow, A method of correlating heat transfer data for surface boiling of liquids, Trans. ASME 74 (1952) 969–976.

[26] H. Tatsumoto, Y. Shirai, K. Hata, T. Kato, M. Shiotsu, Forced convection heat transfer of subcooled liquid nitrogen in horizontal tube, AIP Conf. Proc. 985 (2008) 665–672.

[27] H. Tatsumoto, Y. Shirai, K. Hata, T. Kato, M. Futakawa, M. Shiotsu, Forced convection heat transfer of subcooled liquid nitrogen in a vertical tube, J. Phys. Conf. Ser. 234 (2010) 032057.

[28] Y. Shirai, H. Tatsumoto, M. Shiotsu, K. Hata, H. Kobayashi, Y. Naruo, Y. Inatani, DNB heat flux on inner side of a vertical pipe in forced flow of liquid hydrogen and liquid nitrogen, Cryogenics 92 (2018) 105–117.

[29] S.L. Qi, P. Zhang, R.Z. Wang, L.X. Xu, Flow boiling of liquid nitrogen in micro-tubes: Part I - The onset of nucleate boiling, two-phase flow instability and two-phase flow pressure drop, Int. J. Heat Mass Transf. 50 (2007) 4999–5016.

[30] S.L. Qi, P. Zhang, R.Z. Wang, L.X. Xu, Flow boiling of liquid nitrogen in micro-tubes: Part II - Heat transfer characteristics and critical heat flux, Int. J. Heat Mass Transf. 50 (2007) 5017–5030.

[31] P. Zhang, X. Fu, Two-phase flow characteristics of liquid nitrogen in vertically upward 0.5 and 1.0 mm micro-tubes: visualization studies, Cryogenics 49 (2009) 565–575.

[32] X. Liu, X. Chen, Q. Zhang, S. Wang, Y. Hou, L. Chen, Investigation on CHF of saturated liquid nitrogen flow boiling in a horizontal small channel, Appl. Therm. Eng. 125 (2017) 1025–1036.

[33] S. Chen, X. Chen, L. Chen, Q. Zhang, Y. Hou, Experimental study on the heat transfer characteristics of saturated liquid nitrogen flow boiling in small-diameter horizontal tubes, Exp. Therm. Fluid Sci. 101 (2019) 27–36.

[34] B.C. Zhang, Q.L. Li, Y. Wang, J.Q. Zhang, J. Song, F.C. Zhuang, Experimental investigation of nitrogen flow boiling heat transfer in a single mini-channel, J. Zhejiang Univ. Sci. A 21 (2020) 147–166.

[35] B. Xu, Y. Shi, D. Chen, Z. Yu, Heat transfer characteristics during flow boiling of liquid nitrogen in vertical tube, Huagong Xuebao/CIESC J. 65 (2014) 460–467.

[36] X. Fang, A.M. Sudarchikov, Y. Chen, A. Dong, R. Wang, Experimental investigation of saturated flow boiling heat transfer of nitrogen in a macro-tube, Int. J. Heat Mass Transf. 99 (2016) 681–690.

[37] C.-D. Wen, I. Mudawar, Emissivity characteristics of polished aluminum alloys and assessment of multispectral radiation thermometry (MRT) emissivity models, Int. J. Heat Mass Transf. 48 (2005) 1316–1329.

[38] H.H. Lee, C.R. Kharangate, N. Mascarenhas, I. Park, I. Mudawar, Experimental and computational investigation of vertical downflow condensation, Int. J. Heat Mass Transf. 85 (2015) 865–879.

[39] C.R. Kharangate, I. Mudawar, Review of computational studies on boiling and condensation, Int. J. Heat Mass Transf. 108 (2017) 1164–1196.

[40] J. Lee, L.E. O'Neill, S. Lee, I. Mudawar, Experimental and computational investigation on two-phase flow and heat transfer of highly subcooled flow boiling in vertical upflow, Int. J. Heat Mass Transf. 136 (2019) 1199–1216.

[41] J. Lee, L.E. O'Neill, I. Mudawar, Computational prediction of key heat transfer mechanisms and hydrodynamic characteristics of critical heat flux (CHF) in subcooled vertical upflow boiling, Int. J. Heat Mass Transf. 161 (2020) 120262.

[42] J. Lee, L.E. O'Neill, I. Mudawar, 3-D computational investigation and experimental validation of effect of shear-lift on two-phase flow and heat transfer characteristics of highly subcooled flow boiling in vertical upflow, Int. J. Heat Mass Transf. 150 (2020) 119291.

[43] M. Ahammad, Y. Liu, T. Olewski, L.N. Véchot, M.S. Mannan, Application of computational fluid dynamics in simulating film boiling of cryogens, Ind. Eng. Chem. Res. 55 (2016) 7548–7557.

[44] P. Zhang, H.W. Jia, Evolution of flow patterns and the associated heat and mass transfer characteristics during flow boiling in mini-/micro-channels, Chem. Eng. J. 306 (2016) 978–991.

[45] R. Kumar, A.K. Das, Numerical study of boiling of liquid nitrogen at solid and liquid contact planes, Int. J. Heat Mass Transf. 183 (2022) 122075.

[46] D.A. Gubaidullin, B.A. Snigerev, Numerical simulation of heat transfer during boiling flow of cryogenic fluid in vertical tube, Lobachevskii J. Math. 41 (2020) 1210–1215.

[47] X. Shao, X. Li, R. Wang, Numerical investigation on boiling flow of liquid nitrogen in a vertical tube using bubble number density approach, Heat Mass Transf. 52 (2016) 877–886.

[48] C. Zhu, Y. Li, H. Tan, Numerical study on natural convection of liquid nitrogen used to cool the high-temperature superconducting cable in a new combined energy transmission system, Cryogenics 109 (2020) 103101.

[49] J.H. Wei, L.M. Pan, D.Q. Chen, H. Zhang, J.J. Xu, Y.P. Huang, Numerical simulation of bubble behaviors in subcooled flow boiling under swing motion, Nucl. Eng. 241 (2011) 2898–2908.

[50] Z. Yang, X.F. Peng, P. Ye, Numerical and experimental investigation of two phase flow during boiling in a coiled tube, Int. J. Heat Mass Transf. 51 (2007) 1003–1016.

[51] R. Zhuan, W. Wang, Flow pattern of boiling in micro-channel by numerical simulation, Int. J. Heat Mass Transf. 55 (2012) 1741–1753.

[52] D. Lorenzini, Y. Joshi, Comparison of the volume of fluid and CLSVOF methods for the assessment of flow boiling in silicon microgaps, J. Heat Transf. 139 (2017) 111506.

[53] M. Sussman, E.G. Puckett, A coupled level set and volume-of-fluid method for computing 3D and axisymmetric incompressible two-phase flows, J. Comput. Phys. 162 (2000) 301–337.

[54] M. Sussman, A second order coupled level set and volume-of-fluid method for computing growth and collapse of vapor bubbles, J. Comput. Phys 187 (2003) 110–136.

[55] I. Malgarinos, N. Nikolopoulos, M. Marengo, C. Antonini, M. Gavaises, VOF simulations of the contact angle dynamics during the drop spreading: Standard models and a new wetting force model, Adv. Colloid Interface Sci. 212 (2014) 1–20.

[56] J. Vogel, A. Thess, Validation of a numerical model with a benchmark experiment for melting governed by natural convection in latent thermal energy storage, Appl. Therm. Eng. 148 (2019) 147–159.

[57] J. Lee, I. Mudawar, M.M. Hasan, H.K. Nahra, J.R. Mackey, Experimental and computational investigation of flow boiling in microgravity, Int. J. Heat Mass Transf. 183 (2021) 122237.

[58] R. Mei, J.F. Klausnert, Shear lift force on spherical bubbles, Int. J. Fluid Flow 15 (1994) 62–65.

[59] J.F. Klausner, R. Mei, D.M. Bernhardt, L.Z. Zengt, Vapor bubble departure in forced convection boiling, Int. J. Heat Mass Transf. 36 (1993) 651–662.

[60] V.R. Voller, C. Prakash, A fixed grid numerical modeling methodology for convection-diffusion mushy region phase-change problems, Int. J. Heat Mass Transf. 30 (1987) 1709–1719.

[61] ANSYS INC., ANSYS Fluent Theory Guide 15.

[62] W.H. Lee, A pressure iteration scheme for two-phase flow modeling, Multiph. Transp. Fundam. React. Saf. Appl. 1 (1980) 407–431.

[63] I. Yeo, S. Lee, 2D computational investigation into transport phenomena of subcooled and saturated flow boiling in large length to diameter ratio micro-channel heat sinks, Int. J. Heat Mass Transf. 183 (2022) 122128.

[64] J.U. Brackbill, D.B. Kothe, C. Zemach, A continuum method for modeling surface tension, J. Comput. Phys. 100 (1992) 335–354.

[65] S.L. Sharma, T. Hibiki, M. Ishii, C.S. Brooks, J.P. Schlegel, Y. Liu, J.R. Bunchanan Jr, Turbulence-induced bubble collision force modeling and validation in adiabatic two-phase flow using CFD, Nucl. Eng. 312 (2017) 399–409.

[66] X. Li, W. Wei, R. Wang, Y. Shi, Numerical and experimental investigation of heat transfer on heating surface during subcooled boiling flow of liquid nitrogen, Int. J. Heat Mass Transf. 52 (2009) 1510–1516.

[67] J. Lee, S. Kim, I. Mudawar, Assessment of computational method for highly subcooled flow boiling in a horizontal channel with one-sided heating and improvement of bubble dispersion, Int. J. Therm. Sci. 184 (2023) 107963, doi:10.1016/j.ijthermalsci.2022.107963.

[68] S.J. Darges, V.S. Devahdhanush, I. Mudawar, H.K. Nahra, R. Balasubramaniam, M.M. Hasan, J.R. Mackey, Experimental results and interfacial lift-off model predictions of critical heat flux for flow boiling with subcooled inlet conditions – in preparation for experiments onboard the International Space Station, Int. J. Heat Mass Transf. 183 (2022) 122241.

[69] S.M. Zivi, Estimation of steady-state steam, J. Heat Transf. 86 (2) (1964) 247–251.

[70] K.R. Sagar, H.B. Naik, H.B. Mehta, Numerical study of liquid nitrogen based pulsating heat pipe for cooling superconductors, Int. J. Refrig. 122 (2021) 33–46.

[71] Y. Zheng, H. Chang, J. Chen, H. Chen, S. Shu, Effect of microgravity on flow boiling heat transfer of liquid hydrogen in transportation pipes, Int. J. Hydrog. Energy (2019) 5543–5550.

[72] Y. Umemura, T. Himeno, K. Kinefuchi, Y. Saito, J.W. Hartwig, D.M. Hauser, B. Sakowski, W.L. Johnson, A.C. Leclair, O. Fukasawa, Numerical simulation on liquid hydrogen chill-down process of vertical pipeline, in: Proceedings of the AIAA Propulsion and Energy Forum and Exposition, American Institute of Aeronautics and Astronautics Inc, AIAA, 2019 2019.

[73] Y. Lin, Y. Luo, E.N. Wang, W. Li, W.J. Minkowycz, Enhancement of flow boiling heat transfer in microchannel using micro-fin and micro-cavity surfaces, Int. J. Heat Mass Transf. 179 (2021) 121739.

[74] J. Broughton, Y.K. Joshi, Flow boiling in geometrically modified microchannels, Phys. Fluids 33 (10) (2021) 103308.

[75] F. Dong, Z. Wang, T. Cao, J. Ni, A novel interphase mass transfer model toward the VOF simulation of subcooled flow boiling, Numer. Heat Transf. A Appl. 76 (4) (2019) 220–231.

[76] D. Lorenzini, Y. Joshi, Numerical modeling and experimental validation of two-phase microfluidic cooling in silicon devices for vertical integration of microelectronics, Int. J. Heat Mass Transf. 138 (2019) 194–207.

[77] D. Lorenzini, Y.K. Joshi, Computational fluid dynamics modeling of flow boiling in microchannels with nonuniform heat flux, J. Heat Transf.r 140 (1) (2018).

[78] H.I. Mohammed, D. Giddings, G.S. Walker, CFD simulation of a concentrated salt nanofluid flow boiling in a rectangular tube, Int. J. Heat Mass Transf. 125 (2018) 218–228.

[79] Y.K. Prajapati, M. Pathak, M.K. Khan, Numerical investigation of subcooled flow boiling in segmented finned microchannels, Int. Commun. Heat Mass Transf. 86 (2017) 215–221.

[80] M. Bahreini, A. Ramiar, A.A. Ranjbar, Numerical simulation of subcooled flow boiling under conjugate heat transfer and microgravity condition in a vertical mini channel, Appl. Therm. Eng. 113 (2017) 170–185.

[81] S.C.P. Cheung, S. Vahaji, G.H. Yeoh, J.Y. Tu, Modeling subcooled flow boiling in vertical channels at low pressures - Part 1: Assessment of empirical correlations, Int. J. Heat Mass Transf. 75 (2014) 736–753.

[82] Y.J. Chen, K. Ling, H. Ding, Y. Wang, S.Q. Jin, W.Q. Tao, 3-D numerical study of subcooled flow boiling in a horizontal rectangular mini-channel by VOSET, Int. J. Heat Mass Transf. 183 (2022) 122218.

[83] K. Vontas, M. Andredaki, A. Georgoulas, N. Miché, M. Marengo, The effect of surface wettability on flow boiling characteristics within microchannels, Int. J. Heat Mass Transf. 172 (2021) 121133.

[84] M. Bahreini, A. Ramiar, A.A. Ranjbar, Numerical simulation of bubble behavior in subcooled flow boiling under velocity and temperature gradient, Nucl. Eng. Des. 293 (2015) 238–248.

[85] Y.Q. Zu, Y.Y. Yan, S. Gedupudi, T.G. Karayiannis, D.B.R. Kenning, Confined bubble growth during flow boiling in a mini-/micro-channel of rectangular cross-section part II: approximate 3-D numerical simulation, Int. J. Therm. Sci. 50 (3) (2011) 267–273.